Draft version July 30, 2025
Typeset using LaTeX **twocolumn** style in AASTeX7.0.1

# Resolved Profiles of Stellar Mass, Star Formation Rate, and Predicted CO-to-$H_2$ Conversion Factor Across Thousands of Local Galaxies

Jiayi Sun (孙嘉懿),[1,*] Yu-Hsuan Teng,[2] I-Da Chiang (江宜達),[3] Adam K. Leroy,[4,5] Karin Sandstrom,[6] Jakob den Brok,[7] Alberto D. Bolatto,[2] Jérémy Chastenet,[8] Ryan Chown,[4] Annie Hughes,[9] Eric W. Koch,[7] and Thomas G. Williams[10]

[1] *Department of Astrophysical Sciences, Princeton University, 4 Ivy Lane, Princeton, NJ 08544, USA*
[2] *Department of Astronomy, University of Maryland, 4296 Stadium Drive, College Park, MD 20742, USA*
[3] *Institute of Astronomy and Astrophysics, Academia Sinica, No. 1, Sec. 4, Roosevelt Road, Taipei 106216, Taiwan*
[4] *Department of Astronomy, The Ohio State University, 140 West 18th Avenue, Columbus, OH 43210, USA*
[5] *Center for Cosmology and Astroparticle Physics (CCAPP), 191 West Woodruff Avenue, Columbus, OH 43210, USA*
[6] *Department of Astronomy & Astrophysics, University of California, San Diego, 9500 Gilman Drive, La Jolla, CA 92093, USA*
[7] *Center for Astrophysics | Harvard & Smithsonian, 60 Garden Street, Cambridge, MA 02138, USA*
[8] *Sterrenkundig Observatorium, Universiteit Gent, Krijgslaan 281 S9, B-9000 Gent, Belgium*
[9] *CNRS, IRAP, 9 Av. du Colonel Roche, BP 44346, F-31028 Toulouse cedex 4, France*
[10] *Sub-department of Astrophysics, Department of Physics, University of Oxford, Keble Road, Oxford OX1 3RH, UK*

## ABSTRACT

We present radial profiles of UV-to-IR surface brightness, estimate stellar mass surface density ($\Sigma_\star$) and star formation rate surface density ($\Sigma_{\rm SFR}$), and predict the CO-to-$H_2$ conversion factor ($\alpha_{\rm CO}$) for over 5,000 local galaxies with stellar mass $M_\star \geq 10^{9.3}\,{\rm M}_\odot$. We build these profiles and measure galaxy half-light radii using GALEX and WISE images from the *z*0MGS program, with special care given to highly inclined galaxies. From the UV-to-IR surface brightness profiles, we estimate $\Sigma_\star$ and $\Sigma_{\rm SFR}$ and use them to predict $\alpha_{\rm CO}$ with state-of-the-art empirical prescriptions. We validate our (kpc-scale) $\alpha_{\rm CO}$ predictions against observational estimates, finding the best agreement when accounting for CO-dark gas as well as CO emissivity and excitation effects. The CO-dark correction plays a primary role in lower-mass galaxies, whereas CO emissivity and excitation effects become more important in higher-mass and more actively star-forming galaxies, respectively. We compare our estimated $\alpha_{\rm CO}$ to observed variations in galaxy-integrated SFR to CO luminosity ratio as a function of $M_\star$. A large compilation of literature data suggests that star-forming galaxies with $M_\star = 10^{9.5-11}\,M_\odot$ show strong anti-correlations of ${\rm SFR}/L'_{\rm CO(1-0)} \propto M_\star^{-0.29}$ and ${\rm SFR}/L'_{\rm CO(2-1)} \propto M_\star^{-0.40}$. The estimated $\alpha_{\rm CO}$ trends explain only $\approx$1/3 of these systematic ${\rm SFR}/L'_{\rm CO}$ variations, such that the remaining 2/3 are attributable to changes in the molecular gas depletion time (shorter in lower-mass star-forming galaxies). We publish all data products from this work, including galaxy sizes, UV-to-IR surface brightness profiles, $\Sigma_\star$, $\Sigma_{\rm SFR}$, and $\alpha_{\rm CO}$ estimates.

## 1. INTRODUCTION

Low-$J$ CO rotational transition lines are among the most widely used tracers of molecular gas in galaxies (see reviews by Young & Scoville 1991; Fukui & Kawamura 2010; Heyer & Dame 2015; Saintonge & Catinella 2022). In the local universe, integrated CO measurements exist for thousands of galaxies (e.g., Young et al. 1995; Lisenfeld et al. 2011; Cicone et al. 2017; Saintonge et al. 2017; Colombo et al. 2020; Wylezalek et al. 2022), resolved CO observations cover hundreds of galaxies (e.g., Helfer et al. 2003; Kuno et al. 2007; Leroy et al. 2009; Bolatto et al. 2017; Sorai et al. 2019; Lin et al. 2020; Brown et al. 2021), and there are now over 100 high-resolution CO maps that isolate or even resolve individual molecular clouds across galaxies (e.g., Donovan Meyer et al. 2013; Leroy et al. 2021a; Williams et al. 2023, J. Sun et al., in preparation). These observations have shaped our understanding of the overall abundance, large-scale distribution, and small-scale organization of cold molecular gas, which is the direct fuel for star formation and a key driver of galaxy evolution.

As the collective footprint of CO observations has grown, our understanding of how to infer molecular gas mass from CO emission has also improved (see Bolatto et al. 2013; Schinnerer & Leroy 2024). Many empirical studies made key advances by comparing CO emission to independent gas mass tracers, including far-IR dust emission (e.g., Leroy et al. 2011; Sandstrom et al. 2013; Yasuda et al. 2023; Chiang et al. 2024), or by modeling multi-$J$ CO and CO isotopologue lines to determine

* NASA Hubble Fellow

the underlying physical conditions in the gas (e.g., Israel 2020; Teng et al. 2022, 2023; He et al. 2024). Numerical simulations have also provided important insights on this topic by implementing realistic treatments of CO chemistry and radiative transfer while accounting for observational resolution and sensitivity limits (e.g., Glover & Clark 2012; Narayanan et al. 2012; Gong et al. 2020; Hu et al. 2022).

Thanks to these works, we have now established several key trends in the CO-to-$H_2$ conversion factor, $\alpha_{CO}$, as functions of local gas properties. For example, $\alpha_{CO}$ anti-correlates strongly with gas-phase metallicity, likely due to more abundant "CO-dark" gas in lower metallicity environments (e.g., Glover & Mac Low 2011; Accurso et al. 2017; Gong et al. 2020; Hu et al. 2022). $\alpha_{CO}$ also depends on gas temperature and optical depth, which affect the emissivity of the gas. These variations appear to correlate with the CO line width (e.g., Teng et al. 2024), line intensity (e.g., Narayanan et al. 2012; Gong et al. 2020), and other environmental properties (e.g., stellar or total mass surface density; see Bolatto et al. 2013; Chiang et al. 2024). One can therefore use these more accessible quantities as empirical proxies for CO emissivity variations when direct constraints are not available. Besides, one may also need to account for CO excitation effects that alter the ratio between different CO transitions and thus their corresponding $\alpha_{CO}$ in relation to each other (e.g., Yajima et al. 2021; Leroy et al. 2022; den Brok et al. 2023a; Keenan et al. 2024a; den Brok et al. 2025). As with other factors affecting the CO emissivity, excitation variations appear to correlate with local conditions, especially the surface density of recent star formation.

These studies yield prescriptions that predict $\alpha_{CO}$ from directly observable quantities, including metallicity, the surface densities of stellar mass and recent star formation rate (SFR), and the cloud-scale gas surface density or velocity dispersion. Obtaining estimates of these input variables requires ancillary data beyond just CO mapping, e.g., near-IR images tracing stellar mass, high-resolution millimeter line observations tracing gas kinematics, and/or metallicity estimates. However, not all galaxies targeted for CO observations have such datasets readily available, and many modern CO studies still assume a constant $\alpha_{CO}$ when converting CO emission to molecular gas mass. Unfortunately, this introduces systematic biases and can substantially affect the inferred relationships between gas mass and star formation (Bolatto et al. 2013; also see Sun et al. 2023; Teng et al. 2024; Leroy et al. 2025).

This paper aims to address this problem by providing $\alpha_{CO}$ predictions for thousands of local galaxies. We follow current best practices (Schinnerer & Leroy 2024) and apply the aforementioned empirical $\alpha_{CO}$ calibrations homogeneously to the $z$=0 Multiwavelength Galaxy Synthesis ($z$0MGS; Leroy et al. 2019) dataset. This atlas includes star-forming galaxies more massive than the LMC out to $d \approx 50$ Mpc, and so covers almost all targets in various local universe CO mapping campaigns, including COMING (Sorai et al. 2019), HERACLES (Leroy et al. 2009), the NRO Atlas (Kuno et al. 2007), PHANGS–ALMA (Leroy et al. 2021a,b), as well as VERTICO (Brown et al. 2021) and its high-resolution counterpart MAUVE–ALMA (J. Sun et al., in preparation). Together with the $\alpha_{CO}$ predictions, we produce a variety of intermediate data products, including new estimates of galaxy effective radii and radial profiles of UV-to-IR surface brightness, stellar mass surface density, and SFR surface density. These intermediate calculations can also serve as a basis for more refined $\alpha_{CO}$ estimates as $\alpha_{CO}$ prescriptions and metallicity measurements improve in the future.

Beyond providing $\alpha_{CO}$ estimates for various targets and surveys, this work also aims to offer a population-level view of $\alpha_{CO}$ variations based on current prescriptions. Specifically, we examine how $\alpha_{CO}$ changes as functions of galactocentric radius, galaxy-integrated stellar mass, and star formation rate. This allows us to predict how the ratio of star formation rate to CO luminosity, $\mathrm{SFR}/L'_{CO}$, should vary among galaxies purely due to $\alpha_{CO}$ variations. High values of $\mathrm{SFR}/L'_{CO}$ in low-mass, low-metallicity galaxies have been observed for decades (e.g., Young & Scoville 1991; Saintonge et al. 2011; Schruba et al. 2012; Genzel et al. 2012; Leroy et al. 2013; Hunt et al. 2020), but the degree to which such variations reflect real changes in molecular gas depletion time ($t_{dep} \equiv M_{mol}/\mathrm{SFR}$) or merely $\alpha_{CO}$ is often unclear. Our synthetic calculations provide a basis for interpreting such observations.

The structure of this paper is as follows. Section 2 describes the UV and IR datasets used in this work as well as the procedures for constructing surface brightness radial profiles, converting them into physical properties, and deriving $\alpha_{CO}$ predictions based on empirical prescriptions. Section 3 validates our $\alpha_{CO}$ predictions against observational estimates for various subsets of galaxies in the literature. Section 4 presents key population-level trends in the $\alpha_{CO}$ predictions and examines their physical origins. Section 5 discusses implications for galaxy-integrated molecular gas depletion times. We summarize our main findings and describe the data products in Section 6.

## 2. DATA & METHODS

We work with an extensive sample of local galaxies selected from the $z$0MGS sample (Leroy et al. 2019, hereafter L19). This parent sample includes over 15,000 galaxies in the HyperLEDA database (Makarov et al. 2014), most of which have $B$-band absolute magnitudes $M_B \lesssim -18$ mag (i.e., comparable to or brighter than the LMC) and distances $d \lesssim 50$ Mpc (see figure 19 in L19). Thanks to $z$0MGS, these galaxies have tabulated global properties as well as science-ready GALEX UV and WISE near-/mid-IR images, which allow us to es-

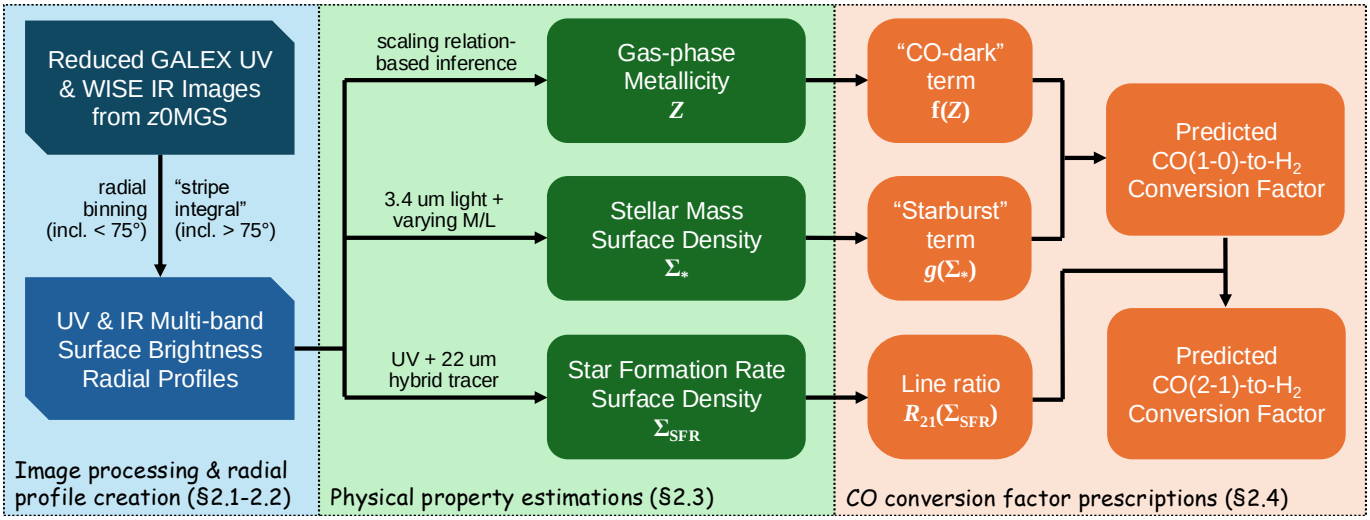


**Figure 1.** Our data processing workflow, from reduced GALEX and WISE images to $\alpha_{CO}$ predictions. Methodological details for the three major steps (image processing and radial profile creation, physical property estimation, and conversion factor prescription) are described in Sections 2.1-2.2, 2.3, and 2.4 respectively.

timate parameters such as stellar mass surface density and SFR surface density that are relevant to CO-to-$H_2$ conversion factor prescriptions.

From the *z*0MGS parent sample, we select galaxies for which it would be possible to estimate the CO (1–0)-to-$H_2$ and CO (2–1)-to-$H_2$ conversion factors following Schinnerer & Leroy (2024, hereafter SL24) and for which we expect those prescriptions to apply. Specifically, we select galaxies with estimated global stellar mass $M_\star > 10^{9.3}\,M_\odot$ (i.e., comparable to or above LMC mass), similar to those galaxies used for calibrating the conversion factor prescriptions (see references in SL24). We also require these galaxies to have known inclination and position angles because our analysis framework requires calculating galactocentric radius (see subsection 2.2 below). We omit M31 and M33 partly due to challenges in processing their data given their enormous sky footprints, and partly because each already has their own conversion factor literature, which has in some cases informed the prescriptions we use (e.g., Leroy et al. 2011; Smith et al. 2012; Gratier et al. 2017; Williams et al. 2019; Forbrich et al. 2020; Viaene et al. 2021). These selection criteria yield a total of 10,657 galaxies.

For each galaxy, we use UV images from GALEX (Martin et al. 2005) and IR images from WISE (Wright et al. 2010) to create UV and IR surface brightness radial profiles. We then convert these observed quantities into physical properties and use them to predict the CO-to-$H_2$ conversion factors. This data processing workflow is illustrated in Figure 1, and the individual steps are detailed in the following subsections.

### 2.1. *UV and IR Images*

We make use of GALEX FUV and NUV images (154 and 231 nm) as well as WISE1 through WISE4 band images (3.4, 4.6, 12, and 22 $\mu$m) that were processed by the *z*0MGS project (L19). These images were background-subtracted and convolved to Gaussian point spread functions (PSFs) of 7.″5 (possible for all bands except WISE4 22 $\mu$m) and 15″ (possible for all bands). The 15″ resolution images reach typical $1\sigma$ noise levels of $\sim 1.5 \times 10^{-4}$ MJy sr$^{-1}$ in the GALEX bands, $\sim 2.5 \times 10^{-3}$ MJy sr$^{-1}$ in the WISE1 3.4 $\mu$m band, and $\sim 1.3 \times 10^{-1}$ MJy sr$^{-1}$ in the WISE4 22 $\mu$m band.

We also use star and galaxy masks published by L19 to mask pixels contaminated by bright foreground stars or other galaxies in the field. However, we do not apply the masks close to galaxy centers because nuclear features in galaxies can sometimes be misidentified as stars and flagged in the masks. Based on visual inspections of the images and masks, we set the overriding area to be within $0.15 \times R_{25}$ of the galaxy center or within one PSF from the galaxy center, whichever is larger.

For a subset of galaxies either located close to the Galactic plane or having close companion galaxies, a substantial fraction (>30%) of their UV/IR images can be masked, making it impractical to extract reliable measurements. This issue is most severe in the WISE1 band (affecting ~3,000 galaxies) but becomes much less concerning in the GALEX FUV and WISE4 bands (only ~200 galaxies). We omit these galaxies in the problematic bands in all following analyses (also see Table 1).

### 2.2. *UV and IR Surface Brightness Profiles*

We build surface brightness radial profiles for each galaxy in each of the GALEX and WISE bands at both 7.″5 and 15″ resolution (which translates to ~1–3 kpc physical scale for most galaxies). For galaxies with inclination angle $i \leq 75°$, we build the radial profiles directly by generating a series of radial bins according to

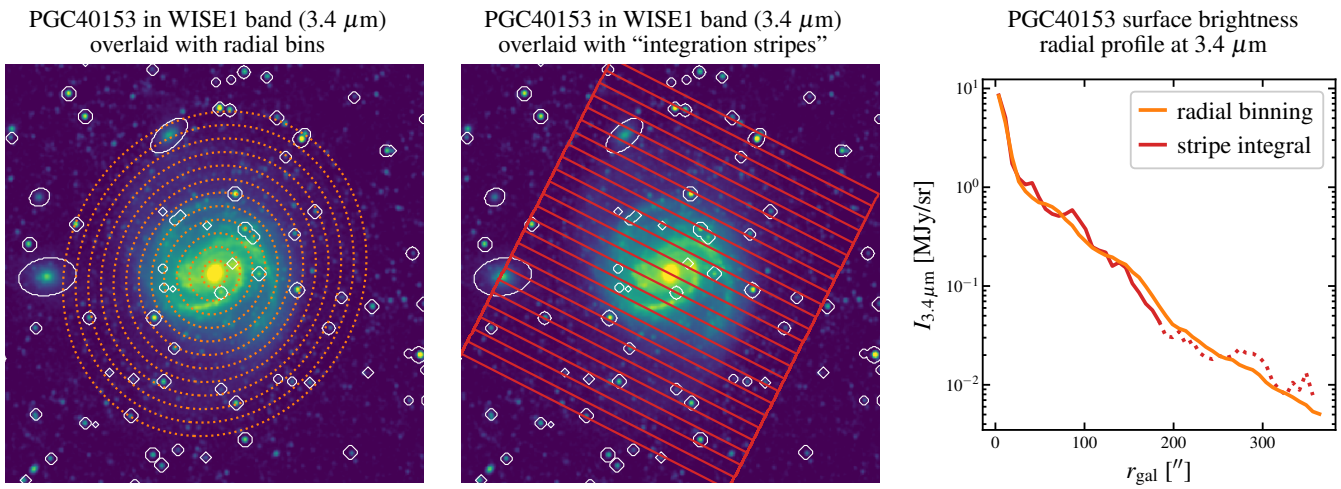


**Figure 2.** The WISE1 band image (*left & middle panels*) and surface brightness radial profiles (*right panel*) for PGC 40153 (a.k.a. NGC 4321, $i = 27°$), as an example of our radial profile construction techniques. A set of elliptical rings (orange dotted lines) in the left panel represent galactocentric radius ($r_{gal}$) bins, in which we directly compute the mean/median surface brightness. A set of long stripes (red rectangles) in the middle panel represent the regions used for "stripe integral" (Warmels 1988), an alternative method for deriving radial profiles that is applicable to even edge-on galaxies (see subsection 2.2). For visual clarity, the densities of bins/stripes are reduced by a factor of four in both panels. Both methods account for masked area due to foreground stars or other galaxies (white ellipses). As shown by the right panel, the radial profiles derived with both methods agree well out to large $r_{gal}$, even after the stripe integral-based results drop below $3\sigma$ significance (red dotted curve).

the inclination and position angle of the galaxy (see Figure 2 left panel). The radial bin width matches the half-width-half-maximum (HWHM) of the Gaussian PSF to appropriately sample the corresponding image. The outermost bin reaches at least $2\,r_{25}$ for each galaxy, and we require a minimum of 10 radial bins to have reasonable coverage even for the smallest galaxies. We then calculate the mean and median surface brightness within each bin as well as the corresponding uncertainty via standard error propagation. Finally, we multiply these numbers by $\cos i$ to derive inclination-corrected surface brightness measurements and errors.

For galaxies with inclination $i > 75°$, direct radial binning is no longer reliable — the exact inclination angle is challenging to measure in this regime, and the surface brightness profile becomes largely unresolved along the galactic minor axis in many cases. In these cases, we instead use the "stripe integral" technique (Warmels 1988) to reconstruct the radial surface brightness profiles. In short, we calculate integrated flux densities within a series of "integration stripes" that align with the galactic minor axis and tile along the major axis (see Figure 2 middle panel). Assuming an axisymmetric disk and optically thin emission, we use this set of flux density measurements to derive the radial surface brightness profile via an inverse Abel transform. This method is described in detail in Appendix A.

The stripe integral approach does not require knowledge of the galaxy inclination angle and can be applied to edge-on systems as long as all the assumptions hold. As a check, we compare surface brightness profiles measured from direct radial binning to those inferred with the stripe integral method for relatively face-on galaxies (see Figure 2 right panel for an example). We find that the two approaches yield consistent results for the vast majority of targets. Inconsistent radial profiles typically occur in cases where: (a) the cataloged galaxy inclination and/or position angle are potentially wrong, (b) the surface brightness profile is only marginally resolved in the given band, or (c) the signal-to-noise (S/N) ratio of the detection becomes low, especially far into the galaxy outskirts. While there is no easy solution in the first case, in the latter two cases we either flag the galaxy (when it is unresolved) or the radial bins with low S/N ratio to avoid unreliable measurements in subsequent analyses (see subsubsection 2.2.1 below).

#### 2.2.1. *Galaxy Half-light Radii*

From the surface brightness radial profiles measured with either direct radial binning or stripe integral, we derive the half-light radius (or effective radius, $r_{50}$) of each galaxy in each UV/IR band. This involves calculating the cumulative flux distribution as a function of galactocentric radius and determining the radius at which it reaches 50% of the galaxy total flux. We use the total fluxes reported in L19 and note that the numbers vary by only ∼0.02 dex with mildly different methodological choices (such as the area for overriding star masks or calculating the cumulative flux, see subsection 2.1–2.2).

**Table 1.** Number of Galaxies with Key Measurements

| Sample Description | $N_{\rm face\text{-}on}/N_{\rm total}$ |
|---|---|
| $z$0MGS parent sample (Leroy et al. 2019) | $-/15,748$ |
| Full sample considered in this work (§2) | $6,868/10,657$ |
| Galaxies with images & surface brightness profiles (§2.1–2.2) | |
| ... for GALEX FUV (154 nm) | $4,826/7,554$ |
| ... for GALEX NUV (231 nm) | $4,747/7,415$ |
| ... for WISE1 (3.4 $\mu$m) | $4,897/7,613$ |
| ... for WISE2 (4.6 $\mu$m) | $5,175/8,053$ |
| ... for WISE3 (12 $\mu$m) | $6,290/9,766$ |
| ... for WISE4 (22 $\mu$m) | $6,708/10,416$ |
| Galaxies with physical measurements or predictions | |
| WISE1 half-light radius (§2.2.1) | $4,848/7,279$ |
| Stellar & SFR surface density profiles (§2.3) | $3,956/5,300$ |
| CO-to-$H_2$ conversion factor profile (§2.4) | $3,919/5,244$ |

NOTE— $N_{\rm face\text{-}on}$ counts galaxies with inclination $i \leq 75°$, for which we have measurements based on direct radial binning; $N_{\rm total}$ counts all galaxies with either direct radial binning or stripe integral-based measurements (see §2.2).

For galaxies with sizes comparable to or smaller than the image resolution, the calculated $r_{50}$ can be biased high because the galaxy radial profiles are not well resolved. To address this issue, we generate mock galaxies with varying sizes and inclination angles, convolve their images to the typical data resolution we work with, measure $r_{50}$ with the method described above, and compare those measurements with the ground truth values (see Appendix B for more details). This exercise produces a correction factor that depends on the ratio of the measured radius to the PSF size, $r_{50,\,\rm obs}/\theta_{\rm PSF}$, and for radial profiles (but not stripe integral-based sizes) the galaxy inclination angle. We calculate this factor for each profile and scale $r_{50,\,\rm obs}$ accordingly. This yields our best estimate $r_{50}$ corrected for the effects of resolution.

We flag a small subset of galaxies whose $r_{50}$ measurements are deemed unreliable for one of the following reasons: (1) the surface brightness profile drops below $3\sigma$ significance (per bin) before reaching $r_{50}$, which leads to large error on the $r_{50}$ measurement; (2) the inferred $r_{50}$ lies within the first radial bin, which means their surface brightness profile is completely unresolved; or (3) the galaxy is marginally resolved, but the estimated resolution bias correction on $r_{50}$ is larger than a factor of 2, in which case the error on $r_{50}$ would be too large after correction (see Appendix B). The fraction of flagged galaxies varies across different bands and differs between the radial binning-based sizes and the stripe integral-based ones. For the WISE1 band at $7\farcs5$ resolution, in total $< 10\%$ of galaxies with stripe integral-based profiles are flagged, and $< 1\%$ of those with radial binning-based profiles are flagged (see Table 1).

### 2.3. *From Observed Quantities to Physical Properties*

Based on the measured surface brightness radial profiles and half-light radii for each galaxy, we calculate the star formation rate (SFR) surface density, stellar mass surface density, and gas-phase metallicity, all of which are input parameters for the SL24 conversion factor prescription. We summarize the key steps below and refer interested readers to L19 and Sun et al. (2022) for detailed descriptions.

We derive SFR surface densities ($\Sigma_{\rm SFR}$) from GALEX UV and WISE mid-IR surface brightnesses closely following L19 (see Table 7 and appendix therein). By default, we combine GALEX FUV (154 nm) with WISE4 (22 $\mu$m) to trace both exposed and obscured star formation. For targets without GALEX FUV data, we combine GALEX NUV (231 nm) with WISE4 whenever NUV is available. We resort to a WISE4-only calibration when neither FUV nor NUV data is available. Due to the use of WISE4 data, our $\Sigma_{\rm SFR}$ results are only estimated at $15''$ resolution.

We derive stellar mass surface densities ($\Sigma_\star$) based on WISE1 3.4 $\mu$m surface brightness profiles ($I_{3.4\mu\rm m}$) at $7\farcs5$ resolution and a radially varying stellar mass-to-light (M/L) ratio. We estimate the latter from the local $\Sigma_{\rm SFR}$-to-$I_{3.4\mu\rm m}$ ratio, following an empirical calibration presented in L19 (Table 6 therein). This method accounts for M/L trends associated with varying stellar population ages across galaxies.

We further apply a S/N > 3 threshold (per radial bin) on the derived $\Sigma_{\rm SFR}$ and $\Sigma_\star$ radial profiles, so that low-significance measurements are considered non-detections

instead. Given this threshold, a fraction of galaxies do not have significant $\Sigma_{\rm SFR}$ or $\Sigma_\star$ measurements in any radial bins. This is mainly due to the limited sensitivity of the WISE4 images, which are directly used for $\Sigma_{\rm SFR}$ and indirectly affects the M/L ratio and therefore $\Sigma_\star$. Among the galaxies with measured surface brightness profiles in all relevant GALEX and WISE bands, 5,300 galaxies have significant $\Sigma_{\rm SFR}$ and $\Sigma_\star$ measurements; 3,956 out of these 5,300 targets have low or moderate inclination ($i \leq 75^\circ$) and therefore have direct radial binning measurements (see subsection 2.2).

For gas-phase metallicity ($Z$), since direct measurements are not available for the majority of galaxies in our sample, we rely on empirical scaling relations to estimate metallicity following Sun et al. (2020, 2022). Specifically, we use the galaxy global stellar mass published in L19 to estimate the metallicity at $r = r_{50}$ in each galaxy, following the mass-metallcity relation measured by the SAMI survey (Sánchez et al. 2019). We then use our measured $r_{50}$ in WISE1 band from subsection 2.2 and a radial metallicity gradient of $-0.1\,{\rm dex}/r_{50}$ (from CALIFA; Sánchez et al. 2014) to derive the implied metallicity elsewhere in the galaxy. For these calculations, we adopt the O3N2 metallicity calibration (Pettini & Pagel 2004) and a solar value of $12 + \log({\rm O/H}) = 8.69$ dex (Asplund et al. 2009).

This approach allows us to obtain uniform metallicity estimates across the full sample. Considering that the $z$0MGS parent sample covers similar galaxy populations as the SAMI and CALIFA surveys (in terms of stellar mass range etc.), our metallicity estimates should statistically match the average trends seen in IFU-based metallicity measurements across many galaxies. That being said, there are appreciable galaxy-to-galaxy variations in both the mass-metallicity relation and the radial metallicity gradient (e.g., see Kreckel et al. 2019; Sánchez 2020), so that we do not necessarily expect our scaling relation-based estimates to perfectly match the observed trends in individual galaxies. For studies that focus on smaller sets of galaxies with uniform optical IFU coverage (e.g., EDGE-CALIFA, PHANGS, MAUVE, KILOGAS; Sánchez et al. 2013; Kreckel et al. 2019; Catinella et al. 2025), it is possible to improve upon our approach by directly incorporating emission line-based metallicity measurements.

### 2.4. *Conversion Factor Prescriptions*

We predict CO-to-$H_2$ conversion factors for both CO (1–0) and CO (2–1) lines with a prescription recommended by SL24. This prescription involves three terms that account for the effects of CO-dark gas, CO emissivity variations, and CO excitation effects, respectively. The "CO-dark" term is parameterized as a function of the gas-phase metallicity $Z$:

$$f(Z) = (Z/Z_\odot)^{-1.5} \quad (\text{for } 0.2 < Z/Z_\odot < 2). \tag{1}$$

Here, the power-law slope of $-1.5$ is recommended by SL24 and broadly consistent with various observational constraints from C II, dust, and gas depletion time measurements (e.g., Schruba et al. 2012; Amorín et al. 2016; Accurso et al. 2017; Hunt et al. 2020). We also calculate an alternative $f(Z)_{\rm G20}$ with a shallower power law index of $-0.8$ (following Gong et al. 2020) for comparison, as numerical simulation studies often predict relatively shallow slopes (also see Glover & Clark 2012; Hu et al. 2022). Considering that Equation 1 is mostly calibrated for $Z \sim 0.2{-}2.0\,Z_\odot$, we limit the power-law dependence to within this metallicity range and use the boundary values outside this range[11] (i.e., use $f(2Z_\odot)$ at $2.5\,Z_\odot$).

The "emissivity" term aims at capturing variations in CO optical depth and/or excitation temperature. Following Bolatto et al. (2013) and Chiang et al. (2024), it is parameterized as a function of the local stellar mass surface density $\Sigma_\star$:

$$g(\Sigma_\star) = \left(\frac{\Sigma_\star}{100\,{\rm M_\odot\ pc^{-2}}}\right)^{-0.25} \quad (\text{for } \Sigma_\star > 100\,{\rm M_\odot\ pc^{-2}}). \tag{2}$$

The power-law index of $-0.25$ originates from Chiang et al. (2024) based on CO (1–0) data, though a steeper $-0.5$ slope was suggested by Bolatto et al. (2013) based on mostly CO (2–1) data. We calculate both in this work for comparisons. In either case, this $g(\Sigma_\star)$ term is only in effect at $\Sigma_\star > 100\,{\rm M_\odot\ pc^{-2}}$, where substantial changes in CO emissivity tend to occur based on empirical data (Bolatto et al. 2013; Chiang et al. 2024).

The CO line ratio $R_{21} \equiv I_{\rm CO(2-1)}/I_{\rm CO(1-0)}$ also varies with excitation condition. SL24 suggested a parameterization involving the local SFR surface density $\Sigma_{\rm SFR}$:

$$R_{21}(\Sigma_{\rm SFR}) = 0.65\left(\frac{\Sigma_{\rm SFR}}{0.018\,{\rm M_\odot\ yr^{-1}\ kpc^{-2}}}\right)^{0.125} \quad (\text{for } 0.35 < R_{21} < 1.0). \tag{3}$$

The 0.125 power law index recommended by SL24 is updated from Leroy et al. (2022) and broadly agrees with other studies in the literature (e.g., den Brok et al. 2021; Yajima et al. 2021; den Brok et al. 2025). The predicted $R_{21}(\Sigma_{\rm SFR})$ value is required to be no smaller than 0.35 and no larger than 1.0, following SL24 and reflecting the range of $R_{21}$ values seen in most observations.

We combine all three terms described above to derive the conversion factors for both CO (1–0) and CO (2–1):

$$\alpha_{\rm CO(1-0)} = \alpha^{\rm MW}_{\rm CO(1-0)}\, f(Z)\, g(\Sigma_\star)\ , \tag{4}$$

$$\alpha_{\rm CO(2-1)} = \alpha^{\rm MW}_{\rm CO(1-0)}\, f(Z)\, g(\Sigma_\star)\, R_{21}(\Sigma_{\rm SFR})^{-1}\ , \tag{5}$$

[11] Note that metallicity values beyond $0.2{-}2.0\,Z_\odot$ are very rare in our sample, partly due to the sample selection scheme (especially $M_\star > 10^{9.3}\,{\rm M_\odot}$; see section 2).

where $\alpha_{\rm CO(1-0)}^{\rm MW} = 4.35\,{\rm M_\odot\ pc^{-2}\ (K\ km\ s^{-1})^{-1}}$ is the commonly adopted Galactic value. We feed the $Z$, $\Sigma_\star$ and $\Sigma_{\rm SFR}$ profiles calculated in subsection 2.3 into Equation 4–5 to derive both $\alpha_{\rm CO(1-0)}$ and $\alpha_{\rm CO(2-1)}$ as functions of galactocentric radius in each galaxy.

We emphasize that these $\alpha_{\rm CO}$ predictions should be viewed to have effective resolution of $\gtrsim$kpc scales. This is not only because the input GALEX and WISE images are at these resolution (see subsection 2.1), but also because the SL24 $\alpha_{\rm CO}$ prescriptions were largely motivated by and calibrated against kpc-scale measurements (see references therein). Although we do expect $\alpha_{\rm CO}$ to vary on smaller, $\lesssim$100 pc scales and have seen evidence for that in simulations and observations (e.g., Gong et al. 2018; Teng et al. 2022, 2023), our $\alpha_{\rm CO}$ predictions are not designed to capture such variations, but rather to reflect (flux-weighted) average values over $\gtrsim$kpc area.

## 3. COMPARISONS TO CONVERSION FACTOR MEASUREMENTS IN THE LITERATURE

To verify the reliability of our $\alpha_{\rm CO}$ predictions, we compile observational measurements of $\alpha_{\rm CO}$ from the literature (Sandstrom et al. 2013; Israel 2020; Teng et al. 2022, 2023; den Brok et al. 2023a; Yasuda et al. 2023; Chiang et al. 2024). Some of these works even helped motivate and calibrate the SL24 prescription in the first place. They all focus on smaller sets of nearby galaxies within our sample, making it possible to directly benchmark our $\alpha_{\rm CO}$ predictions using these galaxies. They also rely on different types of observations and employ different methods to measure $\alpha_{\rm CO}$, as detailed below:

- *Sandstrom et al. (2013, dust-based):* This work combines CO (2–1), H I, and far-IR dust observations to simultaneously solve for $\alpha_{\rm CO}$ and the dust-to-gas (D/G) ratio in 26 galaxies. These measurements have an effective resolution of 75″ (i.e., size of "solution pixels" therein). Solely based on CO (2–1) data, the $\alpha_{\rm CO}$ measurements are essentially $\alpha_{\rm CO(2-1)}$, although they were expressed as $\alpha_{\rm CO(1-0)}$ assuming a fixed $R_{21}$.
- *den Brok et al. (2023a, dust-based):* This work combines CO, H I, and dust data to solve for $\alpha_{\rm CO}$ and D/G ratio in two galaxies (M51 and M101). The method closely follows Sandstrom et al. (2013), and the effective resolution is also 75″. Both $\alpha_{\rm CO(1-0)}$ and $\alpha_{\rm CO(2-1)}$ are determined in this work as it incorporates both CO (1–0) and CO (2–1) data.
- *Yasuda et al. (2023, dust-based)*: This work combines CO (1–0), H I, and dust data to solve for $\alpha_{\rm CO}$ and D/G ratio for 22 galaxies. The method largely follows Sandstrom et al. (2013), except that it measures one $\alpha_{\rm CO}$ value per galaxy, within an effective area that varies from galaxy to galaxy. Only $\alpha_{\rm CO(1-0)}$ is available as no CO (2–1) data were used.
- *Chiang et al. (2024, dust-based):* This work combines CO, H I, dust, and metallicity measurements to derive $\alpha_{\rm CO}$ for 25 galaxies with CO (1–0) and 28 galaxies with CO (2–1). The effective resolution of these measurements are 2 kpc in physical scale, or 20″−200″ in angular size depending on the distance to each galaxy. $\alpha_{\rm CO(1-0)}$ and $\alpha_{\rm CO(2-1)}$ are measured for galaxies with CO (1–0) and CO (2–1) data, respectively.
- *Israel (2020, carbon budget accounting)*: This work compiles multi-$J$ CO, [C I], and [C II] line data to account for the overall carbon budget and derive $\alpha_{\rm CO}$ for 69 galaxies. These measurements are for the central ∼20″ in each galaxy. With $R_{21}$ measured from observations, this work effectively determines both $\alpha_{\rm CO(1-0)}$ and $\alpha_{\rm CO(2-1)}$ at the same time.
- *Teng et al. (2022, 2023, LVG modeling):* These works model multi-$J$ CO and CO isotopologue lines to constrain the gas physical conditions and $\alpha_{\rm CO}$ in the center of three galaxies (NGC 3351, 3627, and 4321). Although the original measurements have high native resolution (∼1″), we use flux-weighted $\alpha_{\rm CO}$ values across the entire central ∼30″ in these galaxies for comparisons with our $\alpha_{\rm CO}$ predictions. Both $\alpha_{\rm CO(1-0)}$ and $\alpha_{\rm CO(2-1)}$ are available from these works.

We compare these $\alpha_{\rm CO}$ measurements with our predictions *at matched effective resolution*. That is, for each target from each literature work, we "rebin" its predicted $\alpha_{\rm CO}$ radial profiles by merging every $N$ radial bins into one wider bin, such that the new bin width matches the effective resolution of the observational measurements. We calculate a weighted[12] average $\alpha_{\rm CO}$ value across the contributing radial bins to determine the appropriate $\alpha_{\rm CO}$ prediction for each new, wider bin. These "rebinned" predictions are then compared with the median value of observational $\alpha_{\rm CO}$ measurements falling inside each (new) radial bin.

### 3.1. *CO (1–0) Conversion Factor*

Figure 3 shows these comparisons for $\alpha_{\rm CO(1-0)}$. To assess the effect of each term in Equation 4, we show four versions of $\alpha_{\rm CO(1-0)}$ predictions. The first shows only the metallicity term. The other three show both metallicity and emissivity terms, but vary each term between our fiducial prescription and alternative, commonly adopted literature prescriptions.

The version without an emissivity term, i.e., $\alpha_{\rm CO(1-0)} = \alpha_{\rm CO(1-0)}^{\rm MW} f(Z)$, matches the observations reasonably well at the high $\alpha_{\rm CO}$ end, which mostly correspond to intermediate to large galactocentric radii. However, this version of the $\alpha_{\rm CO(1-0)}$ prediction exhibits a limited dynamic range of $3-7\,{\rm M_\odot\ pc^{-2}\ (K\ km\ s^{-1})^{-1}}$ and is not able to capture the wide range of measured

[12] We use the WISE3 12 $\mu$m flux (which strongly correlates with CO; see Chown et al. 2021) as the weight for each bin, so that each bin is approximately weighted by the expected total CO flux it encloses.

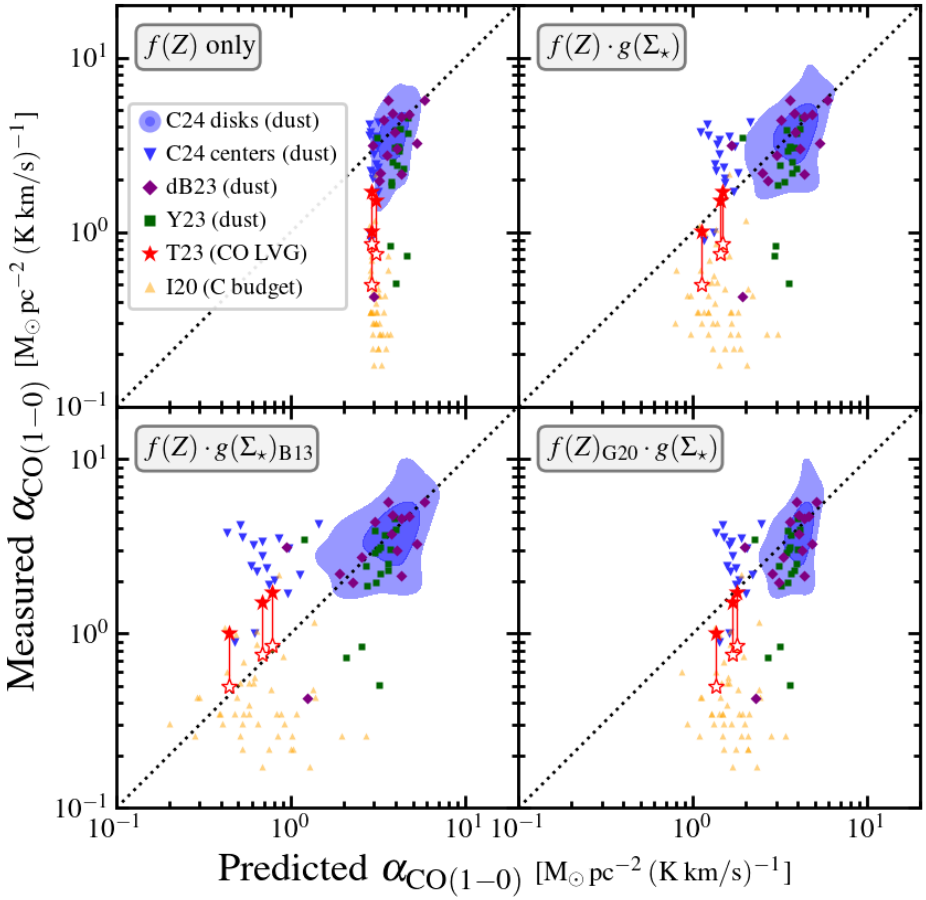


**Figure 3.** Comparing four versions of CO (1–0)-to-$H_2$ conversion factor predictions ($x$-axes) with observational estimates from the literature ($y$-axis). The latter include dust-based estimates across many galaxies presented in den Brok et al. (2023a, dB23), Yasuda et al. (2023, Y23), and Chiang et al. (2024, C24), as well as CO multi-line modeling (i.e., LVG) by Teng et al. (2023, T23) and carbon budget accounting by Israel (2020, I20) in galaxy centers. Note that the blue contours and downward triangles separately show measurements in galaxy disks and centers from Chiang et al. (2024); the filled and open stars show two versions of results from Teng et al. (2023) assuming CO/$H_2$ abundance ratios of $1.5\times10^{-4}$ and $3\times10^{-4}$, respectively. *Top left:* The metallicity-dependent CO-dark term $f(Z)$ alone only spans a limited dynamic range, thus failing to match low $\alpha_{\rm CO(1-0)}$ values from observational estimates in galaxy centers. *Top right:* A combination of the $f(Z)$ term and a $\Sigma_\star$-dependent emissivity term $g(\Sigma_\star)$ matches dust-based and LVG-based estimates well but still disagrees with carbon budget accounting results (Israel 2020). *Bottom left:* Adopting an alternative emissivity term $g(\Sigma_\star)_{\rm B13}$ (Bolatto et al. 2013) results in lower $\alpha_{\rm CO(1-0)}$ than most estimates for galaxy centers though still moderately higher than those from Israel (2020). *Bottom right:* An alternative CO-dark term $f(Z)_{\rm G20}$ (Gong et al. 2020) yields similar results as the fiducial choice (top right), though the weaker metallicity dependence in $f(Z)_{\rm G20}$ leads to slightly more underestimated $\alpha_{\rm CO}$ at the high end (i.e., in outer galaxy disks).

values, which span $\sim$0.2$-$10 $M_\odot$ pc$^{-2}$ (K km s$^{-1}$)$^{-1}$. This mismatch between predicted and estimated $\alpha_{CO(1-0)}$ is particularly pronounced at low galactocentric radii (i.e., near galaxy centers) where the observed $\alpha_{CO(1-0)}$ tends to be much lower than the $f(Z)$-only prediction, as highlighted by the Israel (2020) and Teng et al. (2023) measurements.

Including an emissivity term in the $\alpha_{CO}$ predictions leads to much better agreement with the low $\alpha_{CO(1-0)}$ values observed in galaxy centers. With the fiducial functional form suggested by SL24 (i.e., Equation 2), the predicted $\alpha_{CO(1-0)}$ agrees well with most dust-based estimates over a wider dynamic range (see Figure 3 top right); it also matches the LVG-based estimates when adopting a CO/$H_2$ abundance ratio of $1.5\times10^{-4}$ following Teng et al. (2024, see filled stars in Figure 3). However, the predicted values are still systematically higher than $\alpha_{CO(1-0)}$ estimates by Israel (2020) based on carbon budget accounting[13]. This reflects an apparent tension between Israel (2020) and dust-based studies like Chiang et al. (2024), especially since the galaxy samples examined by these works overlap substantially.

Given this unresolved tension in the literature, we experiment with an alternative version of the emissivity term, with a steeper power law slope ($-0.5$) suggested by Bolatto et al. (2013). As Figure 3 bottom left panel shows, this alternative prescription yields $\alpha_{CO(1-0)}$ predictions that are substantially lower than most dust-based estimates in galaxy centers. It may be consistent with LVG-based estimates provided that a higher CO/$H_2$ abundance ratio of $3\times10^{-4}$ is assumed. Nevertheless, the predictions are still higher than the Israel (2020) estimates. To make them align, an even steeper slope would be required for the emissivity term, and the discrepancies with the dust-based and LVG-based results would become more severe (also see Downes & Solomon 1998; Dunne et al. 2022).

We also experiment with an alternative CO-dark term with a shallower power-law index, as suggested by Gong et al. (2020). It appears to yield similar results as the fiducial functional form (Figure 3 top right versus bottom right), although it tends to slightly underestimate $\alpha_{CO}$ in outer galaxy disk regions. Overall, the current set of $\alpha_{CO}$ measurements does not provide strong differentiating power between these CO-dark corrections.

### 3.2. *CO (2–1) Conversion Factor*

Figure 4 shows predictions of $\alpha_{CO(2-1)}$ in comparison to observational estimates from the literature. The set of literature results included here are similar to Figure 3, except that we omit Yasuda et al. (2023, since this work did not measure $\alpha_{CO(2-1)}$) and include additional dust-based $\alpha_{CO(2-1)}$ estimates by Sandstrom et al. (2013).

Similar to the $\alpha_{CO(1-0)}$ case, the observational estimates for $\alpha_{CO(2-1)}$ span a wide dynamic range of $\sim$0.2$-$20 $M_\odot$ pc$^{-2}$ (K km s$^{-1}$)$^{-1}$. This is not captured by $\alpha_{CO(2-1)}$ predictions that account for only the metallicity-dependent CO-dark term (i.e., omitting the emissivity term and adopting $R_{21,\,\rm const} = 0.65$; Figure 4 left panel). Even though this approach gives a reasonable normalization for most measurements outside galaxy centers (e.g., going through the middle of the "disk" measurements from Chiang et al. 2024), it tends to under-predict measurements in galaxy outskirts (i.e., the high $\alpha_{CO(2-1)}$ end) and severely over-predict in galaxy centers (the low $\alpha_{CO(2-1)}$ end).

Including the fiducial emissivity term brings the predictions into better agreement with most observations in galaxy centers (Figure 4 middle panel). Nonetheless, the aforementioned tension between the dust-based method and carbon budget accounting is also present for $\alpha_{CO(2-1)}$, such that the predictions cannot match both at the same time. Besides, when incorporating both the CO-dark and emissivity terms but assuming a fixed line ratio of $R_{21,\,\rm const} = 0.65$, the predictions are still lower than observational estimates at the high $\alpha_{CO(2-1)}$ end.

The full prescription with all three terms (i.e., Equation 5) shows the best agreement with most observational estimates (Figure 4 right panel). The varying $R_{21}$ term is needed for achieving this agreement at the high $\alpha_{CO(2-1)}$ end as $R_{21}$ often decreases systematically towards galaxy outskirts as $\alpha_{CO}$ increases (e.g., den Brok et al. 2021; Yajima et al. 2021; Leroy et al. 2022). This is supported by the reduced scatter around the identity line when including the $R_{21}$ term (e.g., from 0.19 to 0.17 dex for the "disk" measurements from Chiang et al. 2024). The variable $R_{21}$ term also helps in the case of galaxy centers, where $R_{21}$ can sometimes approach its thermal value ($\sim$1). The general effects of $R_{21}$ variations on $\alpha_{CO(2-1)}$ are relatively mild, as $R_{21}$ has a very narrow dynamic range ($\sim$0.3$-$1); these effects can nevertheless become evident over a sizable sample of galaxies (also see subsection 4.1–4.2 and Keenan et al. 2024a).

### 3.3. *Path to Better Conversion Factor Recipes*

The comparisons between $\alpha_{CO}$ prescriptions and measurements in subsection 3.1–3.2 highlight several aspects where future improvements are needed. For example, the CO-dark gas term is critical to understanding $\alpha_{CO}$ variations in galaxies over a wide stellar mass range and as a function of radius within galaxies (also see section 4 below). A recurring issue related to this term is the challenge of obtaining precise and preferably direct metallicity estimates for systems where $\alpha_{CO}$ estimates are available or required (see discussion in Chiang et al. 2024). In this sense, the emerging synergies between CO and optical IFU surveys (e.g., EDGE, PHANGS, MAUVE,

[13] It is worth noting that the majority of $\alpha_{CO}$ estimates from Israel (2020) are around the optically thin CO limit of $\alpha_{CO(1-0)} \approx 0.4$ $M_\odot$ pc$^{-2}$ (K km s$^{-1}$)$^{-1}$ (Bolatto et al. 2013, assuming a fiducial CO abundance of $1.5\times10^{-4}$ and an excitation temperature of 50 K), which means they are close to the lowest possible values.

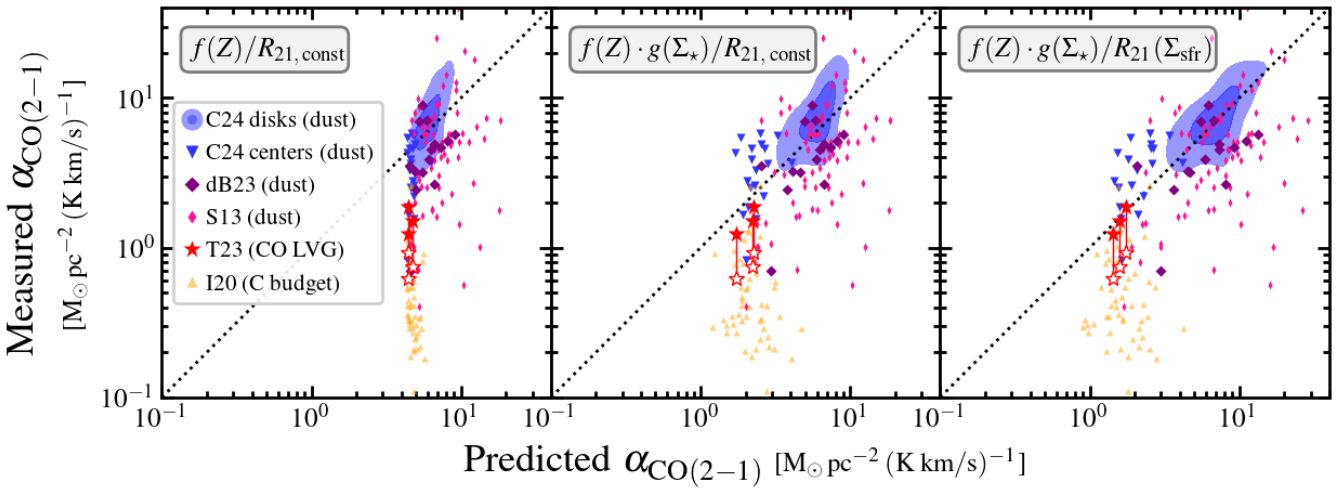


**Figure 4.** Comparing three versions of CO (2–1)-to-$H_2$ conversion factor predictions ($x$-axes) with observational estimates from the literature ($y$-axis). The latter include a similar set of literature results as Figure 3, except omitting $\alpha_{\mathrm{CO}(1-0)}$ estimates by Yasuda et al. (2023) and adding $\alpha_{\mathrm{CO}(2-1)}$ from Sandstrom et al. (2013, S13). *Left & middle:* Assuming a constant line ratio of $R_{21,\,\mathrm{const}} = 0.65$, the CO-dark and emissivity terms in combination can provide a wider range of $\alpha_{\mathrm{CO}(2-1)}$ values and better agreements with observational results than the CO-dark term alone. *Right:* Including a $\Sigma_{\mathrm{SFR}}$-dependent line ratio term on top of the CO-dark and emissivity terms further improves the agreement with observations at both low and high $\alpha_{\mathrm{CO}(2-1)}$ ends.

KILOGAS) will enable a major step forward. The CO-dark gas term is also expected to depend on gas surface density and dust-to-gas ratio in addition to metallicity (e.g., see Bolatto et al. 2013). Here, highly resolved estimates of $\alpha_{\mathrm{CO}}$ across diverse sub-galactic environments in local galaxies will help uncover dependence on secondary parameters.

More generally, we need a more extensive set of high-quality $\alpha_{\mathrm{CO}}$ measurements that span a wide dynamic range in metallicity and galaxy type. This is essential for improving observational constraints on the CO-dark term and narrowing down from the wide range of calibrations present in the literature (e.g., see Schinnerer & Leroy 2024). There are prospects for obtaining these much-needed measurements. In the intermediate term, next-generation facilities that survey the full dust emission SED and the [C II] line emission (e.g., the proposed PRIMA mission; Glenn et al. 2023) will lead to great advances. In the near term, sub-mm surveys of dust emission (with ground-based bolometers; e.g., Holland et al. 2013) and UV/optical observations of nebular and stellar attenuation are also viable paths forward (e.g., Kreckel et al. 2013; Barrera-Ballesteros et al. 2020; Faustino Vieira et al. 2024), albeit with more methodological uncertainty.

For the CO emissivity term, a major issue is that dust-based, LVG-based, and carbon budget accounting methods yield incompatible $\alpha_{\mathrm{CO}}$ estimates in galaxy centers. Given that these methods have been applied to many common targets, a comparative analysis that examines the input datasets and the assumptions underlying each method appears to be a fruitful next step. A larger set of multi-line CO, $^{13}$CO, and [C I] observations will further provide the necessary training data to calibrate CO emissivity prescriptions based on CO line width and other more physically relevant quantities accessible at high resolution (e.g., Teng et al. 2024). Such observations are feasible, though expensive, with current facilities including ALMA.

For CO excitation, there is significant ongoing effort to measure $R_{21}$ and the related line ratios $R_{31}$, and $R_{32}$ across galaxies and spatial scales (e.g., den Brok et al. 2021; Leroy et al. 2022; den Brok et al. 2023a; Keenan et al. 2024b; den Brok et al. 2025; Komugi et al. 2025; Lee et al. 2025; Keenan et al. 2025). Recent studies highlighted $\Sigma_{\mathrm{SFR}}$ as the most promising predictor for $R_{21}$, and similar calibrations are beginning to emerge for the other line ratios (den Brok et al. 2023b; Keenan et al. 2025). Furthermore, simulations suggested that CO line ratios correlates with and may be used as proxies for CO emissivity variations (e.g., Gong et al. 2020). In this sense, improved measurements and understanding of CO excitation effects may also feed back into improved prescriptions for the emissivity term.

## 4. CONVERSION FACTOR VARIATIONS

Based on our $\alpha_{\mathrm{CO}}$ predictions with the SL24 prescriptions, we characterize $\alpha_{\mathrm{CO}}$ variations and trends across the local galaxy population (subsection 4.1–4.2). We are interested in how $\alpha_{\mathrm{CO}}$ depends on galactocentric radius, which captures much of its internal variation within galaxies. We are also interested in the dependence of $\alpha_{\mathrm{CO}}$ on galaxy global stellar mass and SFR. These are among the most fundamental properties in the context of galaxy evolution, and many galaxy-integrated

CO surveys report key results as functions of $M_\star$ and SFR (e.g., Tacconi et al. 2013; Saintonge et al. 2017; Keenan et al. 2024b).

### 4.1. *Conversion Factor Radial Profiles*

We first examine systematic variations in the resolved $\alpha_{CO}$ radial profiles. Leveraging the large sample size, we compute median $\alpha_{CO}$ radial profiles combining many galaxies with similar properties to average out galaxy-to-galaxy variations and distill key systematic trends.

Figure 5 shows median radial profiles of $\alpha_{CO(1-0)}$ and $\alpha_{CO(2-1)}$ for galaxies in various parts of the $M_\star$–SFR parameter space. These median radial profiles are derived for galaxies in bins of $M_\star$ and "offset" from the star-forming main sequence (SFMS; also see Figure 6 top left panel). This offset is defined as

$$\Delta\mathrm{MS} = \log_{10}\mathrm{SFR} - \log_{10}\mathrm{SFR}_{\mathrm{MS}}(M_\star)\ , \qquad (6)$$

where $\mathrm{SFR}_{\mathrm{MS}}(M_\star)$ is the expected SFR at any given $M_\star$ for galaxies on the SFMS. Here we adopt a parameterized fit of the SFMS derived by Leroy et al. (2019) for the parent $z$0MGS sample:

$$\log_{10}\left(\frac{\mathrm{SFR_{MS}}}{\mathrm{M_\odot\ yr^{-1}}}\right) = 0.68\log_{10}\left(\frac{M_\star}{10^{10}\,\mathrm{M_\odot}}\right) - 0.17\ . \quad (7)$$

As such, galaxies with larger $|\Delta\mathrm{MS}|$ values are located further away from the SFMS (as defined by Equation 7) in the $M_\star$–SFR plane.

Figure 5 highlights several key trends. First, galaxies in all $M_\star$ and $\Delta$MS bins show strong radial gradients in $\alpha_{CO(1-0)}$ and $\alpha_{CO(2-1)}$, spanning at least a factor of 2 from $r = 0$ to $>2\,r_{50}$. For relatively massive galaxies ($M_\star > 10^{10}\,\mathrm{M_\odot}$), the $\alpha_{CO(1-0)}$ values can be more than 2 times below or above the nominal Galactic value of $4.35\,\mathrm{M_\odot\ pc^{-2}\ (K\ km\ s^{-1})^{-1}}$. This makes a clear case that accounting for $\alpha_{CO}$ variations is important even when studying a single galaxy.

The median $\alpha_{CO(1-0)}$ radial profiles for lower-mass galaxies ($M_\star < 10^{10}\,\mathrm{M_\odot}$) in all $\Delta$MS bins are consistent with a single exponential relation (i.e., a straight line under $\log(y)$ stretch), implying a 0.15 dex increase in $\alpha_{CO(1-0)}$ when $r$ increases by $r_{50}$. This relation comes directly from the CO-dark term $f(Z)$, which combines a $-0.1\,\mathrm{dex}/r_{50}$ metallicity gradient (see subsection 2.3) with a $Z^{-1.5}$ power-law scaling (Equation 1). The lack of any clear deviation from this simple expectation demonstrates that, for our fiducial prescription, the $\alpha_{CO(1-0)}$ profiles are determined almost solely by the $f(Z)$ term at $M_\star < 10^{10}\,\mathrm{M_\odot}$.

The median $\alpha_{CO(1-0)}$ radial profiles for higher-mass galaxies ($M_\star > 10^{10}\,\mathrm{M_\odot}$) have an overall lower normalization than less massive galaxies – that is, $\alpha_{CO(1-0)}$ appears lower at all given $r/r_{50}$. In addition, the $\alpha_{CO(1-0)}$ profiles are no longer well described by a single exponential profile. Instead, massive galaxies show clear deviations toward lower $\alpha_{CO(1-0)}$ within $r < r_{50}$. This is due to common onset of the emissivity term $g(\Sigma_\star)$ near the centers of higher-mass galaxies, where $\Sigma_\star$ exceeds the $100\,\mathrm{M_\odot\ pc^{-2}}$ threshold (see Equation 2). Meanwhile, the overall $\alpha_{CO(1-0)}$ profiles remain relatively insensitive to $\Delta$MS at $M_\star > 10^{10}\,\mathrm{M_\odot}$, reflecting weak variations in galaxy stellar mass distributions as a function of $\Delta$MS.

The median $\alpha_{CO(2-1)}$ radial profiles show a much stronger dependence on $\Delta$MS, with systematically lower $\alpha_{CO(2-1)}$ (at any given $r/r_{50}$) in galaxies with higher $\Delta$MS. In contrast to the lack of dependence seen for $\alpha_{CO(1-0)}$, this clear $\Delta$MS dependence in $\alpha_{CO(2-1)}$ comes from the line ratio term $R_{21}(\Sigma_{\mathrm{SFR}})$. As galaxies with higher $\Delta$MS generally have higher $\Sigma_{\mathrm{SFR}}$, $R_{21}$ should be higher and $\alpha_{CO(2-1)}$ correspondingly lower.

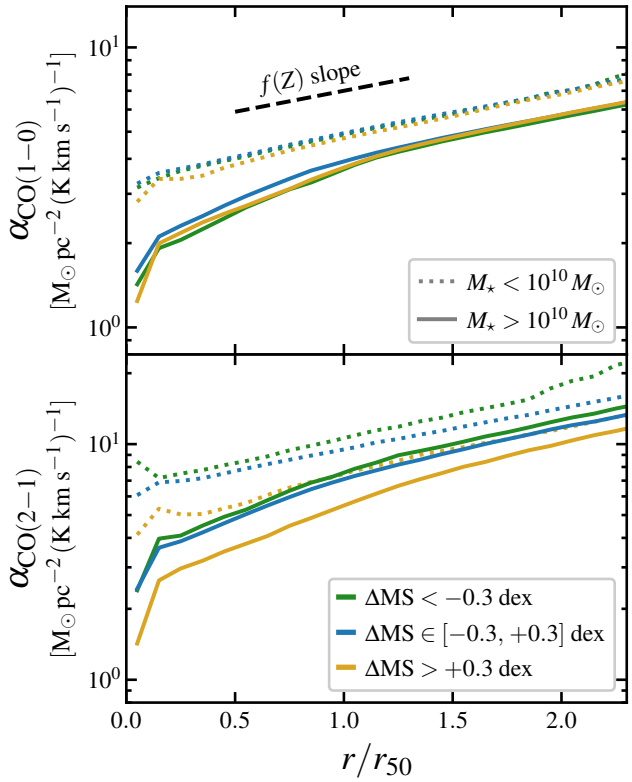


**Figure 5.** Median $\alpha_{CO}$ radial profiles for galaxies grouped by stellar mass ($M_\star$) and offset from the star-forming main sequence ($\Delta$MS; Equation 6). The $x$-axis represents galactocentric radius in units of $r_{50}$ in WISE1 band. In lower-mass galaxies ($M_\star < 10^{10}\,\mathrm{M_\odot}$, dotted lines), the radial profile of $\alpha_{CO(1-0)}$ (*top panel*) is effectively set by the CO-dark term $f(Z)$ alone. In higher-mass galaxies ($M_\star > 10^{10}\,\mathrm{M_\odot}$, solid lines) the radial profile of $\alpha_{CO(1-0)}$ steepens at $r \lesssim r_{50}$ as the emissivity term $g(\Sigma_\star)$ plays a significant role. While the $\alpha_{CO(1-0)}$ radial profiles barely vary with $\Delta$MS (color-coded), the $\alpha_{CO(2-1)}$ radial profiles (*bottom panel*) clearly do depend on this quantity. We predict lower $\alpha_{CO(2-1)}$ in galaxies with higher $\Delta$MS (due to a higher line ratio $R_{21}$).

### 4.2. *Galaxy Global Conversion Factors*

To connect more directly to the literature on *global* galaxy evolution, we compute a global $\alpha_{\rm CO}$ value for each galaxy from the $\alpha_{\rm CO}$ radial profile via a WISE3 flux-weighted average. That is, we use the WISE3 12 $\mu$m flux density in each radial bin (i.e., surface brightness times the radial bin area) as the weight to average $\alpha_{\rm CO}$ over all bins. This averaging scheme is motivated by observational evidence of a strong and almost linear correlation between WISE3 surface brightness and CO line intensity (e.g., Gao et al. 2019; Chown et al. 2021; Gao et al. 2022; Leroy et al. 2023). The WISE3 flux-weighting thus approximates a CO flux-weighting, which is required to correctly convert radial profiles into global $\alpha_{\rm CO}$ values:

$$\alpha_{\rm CO}^{\rm global} \equiv \frac{M_{\rm mol,\,tot}}{L'_{\rm CO,\,tot}} = \frac{\sum_i \alpha_{{\rm CO},i}\, I_{{\rm CO},i}\, A_i}{\sum_i I_{{\rm CO},i}\, A_i} \approx \frac{\sum_i \alpha_{{\rm CO},i}\, I_{12\mu{\rm m},i}\, A_i}{\sum_i I_{12\mu{\rm m},i}\, A_i} \,. \quad (8)$$

Here $\alpha_{{\rm CO},i}$, $I_{{\rm CO},i}$, $I_{12\mu{\rm m},i}$, and $A_i$ denote the conversion factor (for either CO transition), CO line intensity (in K km s$^{-1}$), WISE3 surface brightness (in MJy sr$^{-1}$), and area of the $i$th radial bin. The last step is where the empirical finding of $I_{12\mu{\rm m}} \propto I_{\rm CO}$ comes in.

After obtaining global $\alpha_{\rm CO}$ values for all galaxies, we bin them into regular, logarithmically spaced grids of $M_\star$ and SFR and report the results in the upper panels of Figure 6. The upper left panel shows the distribution of all galaxies with $\alpha_{\rm CO}$ predictions. As expected, most galaxies are located within $\pm$0.5 dex of the SFMS (Equation 7; Leroy et al. 2019), although the sample also includes a small subset of early-type galaxies reaching $\gtrsim$1 dex below the SFMS at the high $M_\star$ end.

The upper middle and right panels of Figure 6 show the variation of $\alpha_{\rm CO(1-0)}$ and $\alpha_{\rm CO(2-1)}$ across the $M_\star$–SFR plane, with the color scale showing the median global $\alpha_{\rm CO}$ value in each $M_\star$–SFR bin. Both panels reveal systematic trends across the $M_\star$ and SFR ranges probed by our sample. Higher $\alpha_{\rm CO}$ values are generally seen towards lower $M_\star$ for both CO transitions. The lowest $\alpha_{\rm CO}$ values are found at intermediate to high $M_\star$ *away* from the SFMS – for CO (1–0) they mostly appear on the very low SFR extreme, whereas for CO (2–1) they appear on both the low and high SFR extremes.

For most of these trends in the global $\alpha_{\rm CO}$ values visible in Figure 6, we can immediately identify corresponding trends in their resolved radial profiles in Figure 5. For example, the lower global $\alpha_{\rm CO(1-0)}$ values in high-mass galaxies partly reflect the overall lower normalization of the $\alpha_{\rm CO(1-0)}$ radial profiles at high $M_\star$ (Figure 5 top panel); the lower global $\alpha_{\rm CO(2-1)}$ values in high-SFR galaxies instead originate from the $\Delta$MS dependence of the normalization of the $\alpha_{\rm CO(2-1)}$ radial profiles (Figure 5 bottom panel). In these cases, what we see in Figure 6 are simply "distilled" versions of the systematic trends that we saw with the resolved $\alpha_{\rm CO}$ radial profiles.

But there is an intriguing trend in Figure 6 that one would *not* obviously expect from Figure 5 — the global $\alpha_{\rm CO(1-0)}$ values appear low in massive galaxies with low SFR or $\Delta$MS. This is in contrast to the *insensitivity* of the resolved $\alpha_{\rm CO(1-0)}$ radial profiles to $\Delta$MS in Figure 5. The reason behind this apparent contrast is the differential weighting of radial bins when deriving global $\alpha_{\rm CO}$ values (Equation 8). That is, massive galaxies with low $\Delta$MS tend to have more centrally concentrated WISE3 12 $\mu$m emission, which means that the inner radial bins with lower $\alpha_{\rm CO}$ would receive more weight, resulting in lower global $\alpha_{\rm CO}$ values for these galaxies. This interesting result is directly relevant to the interpretation of CO emission in lenticular and elliptical galaxies (e.g., Young et al. 2011; Davis et al. 2019). Direct observational constraints on the CO emission radial distribution and conversion factors in these systems would help confirm the predicted trends and refine our understanding of the molecular gas properties therein.

As a further step in understanding and contextualizing the global $\alpha_{\rm CO}$ variations, we show in the lower panels of Figure 6 systematic trends in the CO-dark term $f(Z)$, emissivity term $g(\Sigma_\star)$, and line ratio $R_{21}(\Sigma_{\rm SFR})$ across the same $M_\star-$SFR plane. Here, the galaxy global averages of $f(Z)$, $g(\Sigma_\star)$, $R_{21}(\Sigma_{\rm SFR})$ are computed with the same WISE3 flux-weighting scheme (similar to Equation 8 for $\alpha_{\rm CO}$). The only exception is $R_{21}$, for which we compute a weighted *harmonic mean* instead of arithmetic mean, reflecting the inverse proportionality between $\alpha_{\rm CO(2-1)}$ and $R_{21}$ (see Equation 5).

The lower left panel of Figure 6 shows that the CO-dark term $f(Z)$ varies primarily with $M_\star$, with the highest values appearing at the lowest $M_\star$. This trend is essentially "baked in" by our adopted galaxy mass–metallicity relation (Sánchez et al. 2019) that sets the metallicity "zero point" for each galaxy (i.e., at $r = r_{50}$; see subsection 2.3). Deviations from this dominant trend come from galaxy-to-galaxy variations in $r_{50}$ (which controls the radial metallicity slope; subsection 2.3) and the WISE3 surface brightness profile (which sets the relative weighting of all radial bins). As mentioned above, the lower $f(Z)$ in high mass galaxies below the main sequence primarily reflects their more compact WISE3 distributions compared to galaxies with the same $M_\star$ on the star-forming main sequence.

The lower middle panel of Figure 6 shows that the emissivity term $g(\Sigma_\star)$ is generally "inactive" at low $M_\star$, as already discussed in subsection 4.1. The behavior of $g(\Sigma_\star)$ at the high $M_\star$ and low SFR end mirrors that of $\alpha_{\rm CO(1-0)}$ and $f(Z)$, and the explanation is essentially the same: more centrally concentrated WISE3 emission leads to high weights being assigned to inner radial bins with lower $g(\Sigma_\star)$ values. These trends in $f(Z)$ and $g(\Sigma_\star)$ together drive the systematic variations of $\alpha_{\rm CO(1-0)}$ with $M_\star$ and SFR.

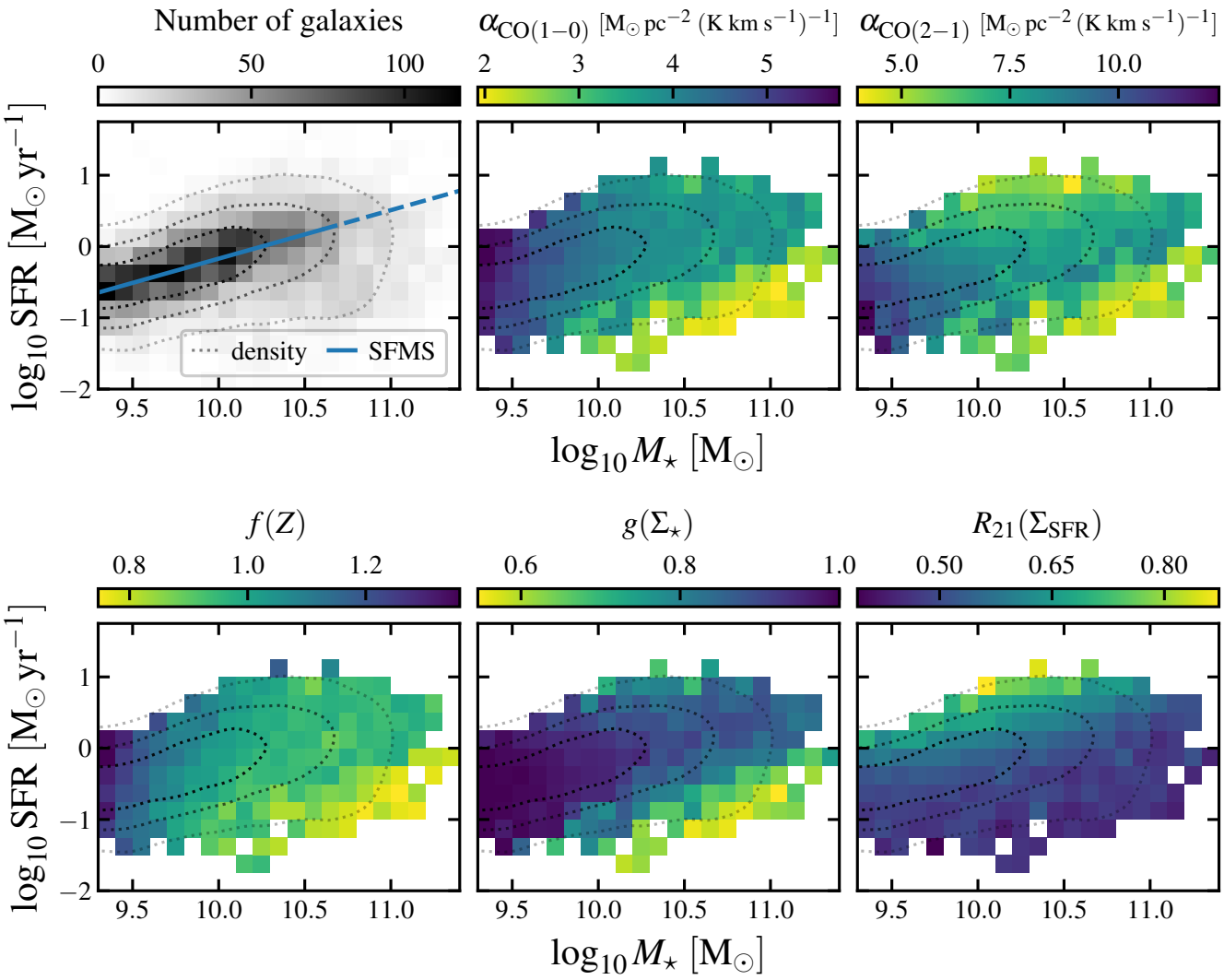


**Figure 6.** Galaxy distribution and the predicted global $\alpha_{CO}$ values across the $M_\star$–SFR plane. *Top left:* 2D histogram (grayscale heatmap) and iso-density contours (dashed curves) of galaxies in our sample. Their distribution mostly centers around the star-forming main sequence at $z \approx 0$ (blue line; Leroy et al. 2019). *Top middle & right:* Predicted galaxy global $\alpha_{CO(1-0)}$ and $\alpha_{CO(2-1)}$ values across the same plane (overlaid with the same density contours as in the top left panel). The highest $\alpha_{CO}$ values appear at the low $M_\star$ end, and the lowest $\alpha_{CO}$ values appear at higher $M_\star$ and *away* from the SFMS. *Bottom:* Variations of the CO-dark, emissivity, and line ratio terms in the SL24 $\alpha_{CO}$ prescriptions. These variations work in concert to drive the systematic trends seen in $\alpha_{CO}$ in the top middle and right panels. Note that the colorbar for $R_{21}$ (*bottom right*) is reversed so that brighter colors still imply lower $\alpha_{CO}$ as in other panels.

The lower right panel of Figure 6 shows that the line ratio $R_{21}(\Sigma_{SFR})$ is mainly correlated with SFR or $\Delta$MS. This is consistent with the latest observations of galaxy global $R_{21}$ reported by Keenan et al. (2024a) for galaxies with a similar range of $M_\star$ and SFR. More quantitatively, the median value in each SFR bin goes from $R_{21} = 0.4$ at SFR $= 0.1$ $M_\odot$ yr$^{-1}$ to 0.8 at 10 $M_\odot$ yr$^{-1}$, also in good agreement with the results of Keenan et al. (2024a). This monotonically increasing trend of $R_{21}$ with SFR and $\Delta$MS explains the difference between $\alpha_{CO(1-0)}$ and $\alpha_{CO(2-1)}$ seen in the upper middle and right panels of Figure 6.

## 5. IMPLICATIONS FOR THE MOLECULAR GAS DEPLETION TIME

The molecular gas depletion time (defined as the ratio of molecular gas mass to star formation rate, $t_{dep} \equiv M_{mol}$ / SFR) and its dependencies on galaxy properties play a central role in our understanding of galaxy evolution (e.g., Tacconi et al. 2020; Saintonge & Catinella 2022). In observational studies, $t_{dep}$ is often derived from the observable CO luminosity ($L'_{CO}$) and SFR

given some assumed $\alpha_{\rm CO}$ values:

$$t_{\rm dep} = \frac{\alpha_{\rm CO}\, L'_{\rm CO}}{\rm SFR} \ . \quad (9)$$

As such, obtaining reliable $t_{\rm dep}$ estimates across galaxies requires understanding how $\alpha_{\rm CO}$ varies among the same galaxy population in the first place.

Our $\alpha_{\rm CO}$ estimates across a large sample of local galaxies allow us to address this problem statistically. We use our $\alpha_{\rm CO}$ predictions to determine how ${\rm SFR}/L'_{\rm CO}$ *should* depend on galaxy stellar mass $M_\star$ if *only* $\alpha_{\rm CO}$ varies while $t_{\rm dep}$ remains fixed. Then we compare this prediction to the observed ${\rm SFR}/L'_{\rm CO}$ versus $M_\star$ trend for a large sample of literature observations. The difference between the observed and predicted trends should reflect the real physical variations in $t_{\rm dep}$ (or inaccuracies in our adopted $\alpha_{\rm CO}$ prescription).

*Observed* ${\rm SFR}/L'_{\rm CO}$–$M_\star$ *relation:* We consider ${\rm SFR}/L'_{\rm CO}$ vs. $M_\star$ for an extensive compilation of integrated galaxy measurements from Leroy et al. (2022, 2023). This compilation includes many surveys targeting either CO (1–0) (e.g., ALMaQUEST, AMIGA, EDGE-CARMA, xCOLDGASS; Kuno et al. 2007; Lisenfeld et al. 2011; Bolatto et al. 2017; Saintonge et al. 2017; Sorai et al. 2019; Lin et al. 2020; Wylezalek et al. 2022) or CO (2–1) (e.g., ALLSMOG, EDGE-APEX, HERACLES, PHANGS–ALMA; Leroy et al. 2009; Bothwell et al. 2014; Jiang et al. 2015; Cicone et al. 2017; Colombo et al. 2020, 2025; Leroy et al. 2021a). These datasets are placed onto a common systems of SFR and $M_\star$ estimates consistent with z0MGS and Salim et al. (2016, 2018), so that the $M_\star$ and SFR for the literature and our sample are directly comparable to each other. From this compilation, we select a subset of galaxies with $M_\star{>}10^{9.3}\,{\rm M}_\odot$ and within ±0.5 dex of the SFMS (Figure 6) to focus on normal star-forming galaxies within the mass range where we predict $\alpha_{\rm CO}$.

We show the observed ${\rm SFR}/L'_{\rm CO}$ versus $M_\star$ trends in the top panels of Figure 7, plotting both CO detections (blue/orange diamonds) and upper limits (blue/orange upward triangles). The running median curves for these observational data (blue/orange solid lines) show a systematic decrease in ${\rm SFR}/L'_{\rm CO}$ of 0.6–0.7 dex over ∼1.5 dex in $M_\star$. Both trends are reasonably described by a power law over the range of $M_\star = 10^{9.5-11}\,{\rm M}_\odot$:

$$\frac{\rm SFR}{L'_{\rm CO(1-0)}} = \frac{10^{-8.37}\,{\rm M}_\odot\ {\rm yr}^{-1}}{\rm K\ km\ s^{-1}\ pc^2} \left(\frac{M_\star}{10^{10}\,{\rm M}_\odot}\right)^{-0.29} , \quad (10)$$

and

$$\frac{\rm SFR}{L'_{\rm CO(2-1)}} = \frac{10^{-8.19}\,{\rm M}_\odot\ {\rm yr}^{-1}}{\rm K\ km\ s^{-1}\ pc^2} \left(\frac{M_\star}{10^{10}\,{\rm M}_\odot}\right)^{-0.40} . \quad (11)$$

The scatters about these relations are 0.3−0.4 dex.

*Predicted* ${\rm SFR}/L'_{\rm CO}$–$M_\star$ *relation:* To construct a predicted trend, we select galaxies in our z0MGS sample within ±0.5 dex of the SFMS (see Figure 6). Then we combine their estimated $\alpha_{\rm CO}$ with an adopted fiducial depletion time $t_{\rm dep,\,fid} = 2$ Gyr to predict ${\rm SFR}/L'_{\rm CO}$ for each galaxy via Equation 9. This $t_{\rm dep,\,fid}$ value is typical among resolved observations of massive, local, star-forming galaxies (e.g., Leroy et al. 2008; Sun et al. 2023), but the exact normalization is not critical because $t_{\rm dep,\,fid}$ only scales the amplitude of ${\rm SFR}/L'_{\rm CO}$ for all galaxies, not its dependence on $M_\star$.

We show the predicted ${\rm SFR}/L'_{\rm CO}$ as a function of $M_\star$ for both CO transitions in the top panels of Figure 7. The galaxy-by-galaxy results (gray dots) and the running median curves (gray dotted lines) both reveal a weak decreasing trend of expected ${\rm SFR}/L'_{\rm CO}$ as a function of $M_\star$. In general, ${\rm SFR}/L'_{\rm CO}$ is predicted to decrease by 0.15–0.25 dex for either CO transition over ∼1.5 dex in $M_\star$. This reflects the anti-correlation between $\alpha_{\rm CO}$ and $M_\star$ already seen in Figure 6. The $1\sigma$ scatter at any given $M_\star$ is ∼0.1 dex.

*Implications:* The observational results shown in Figure 7 represent one of the most complete compilations to date for both CO (1–0) and CO (2–1). The observed trends are strong and continuous over the range of $M_\star = 10^{9.5-11}\,{\rm M}_\odot$, where metallicity does not change by a large amount (for reference, the low end of this range corresponds to approximately the mass of M33 or the LMC). Given that the observed trends in ${\rm SFR}/L'_{\rm CO}$ reflect a mixture of physical variations in $\alpha_{\rm CO}$ and $t_{\rm dep}$, we suggest that its relationship with $M_\star$ should be considered one of the fundamental molecular gas scaling relations. We encourage future surveys to measure this relation explicitly and identify it as a valuable benchmark for numerical simulations that attempt to predict CO emission and star formation rate.

Furthermore, the *predicted* trends from our $\alpha_{\rm CO}$ estimates and a fixed $t_{\rm dep}$ is much weaker than the observed trends. Observations show systematic changes of 0.6−0.7 dex in ${\rm SFR}/L'_{\rm CO}$ as a function of $M_\star$, while our calculations predict only 0.15−0.25 dex over the same $M_\star$ range. Such discrepancies suggest that either our $\alpha_{\rm CO}$ predictions fail to match the amplitude of variations in reality, or $t_{\rm dep}$ is not fixed in reality and varies systematically with $M_\star$.

The most straightforward way to adjust our $\alpha_{\rm CO}$ prediction to explain the observations would be for $f(Z)$ to have a significantly steeper functional form, because metallicity varies primarily with $M_\star$ in our calculations. While not ruled out, this is not currently favored by simulation studies (e.g., Gong et al. 2020; Hu et al. 2022) or observational measurements in low-mass galaxies (see Bolatto et al. 2013; Schinnerer & Leroy 2024, especially the synthesis plots in the latter). For reference, $\alpha_{\rm CO}$ estimates for the LMC and M33, which would sit at the low end of our studied mass range, tend to find values of ∼2 times the Galactic value (e.g., Leroy et al. 2011; Bolatto et al. 2013; Jameson et al. 2016, among others).

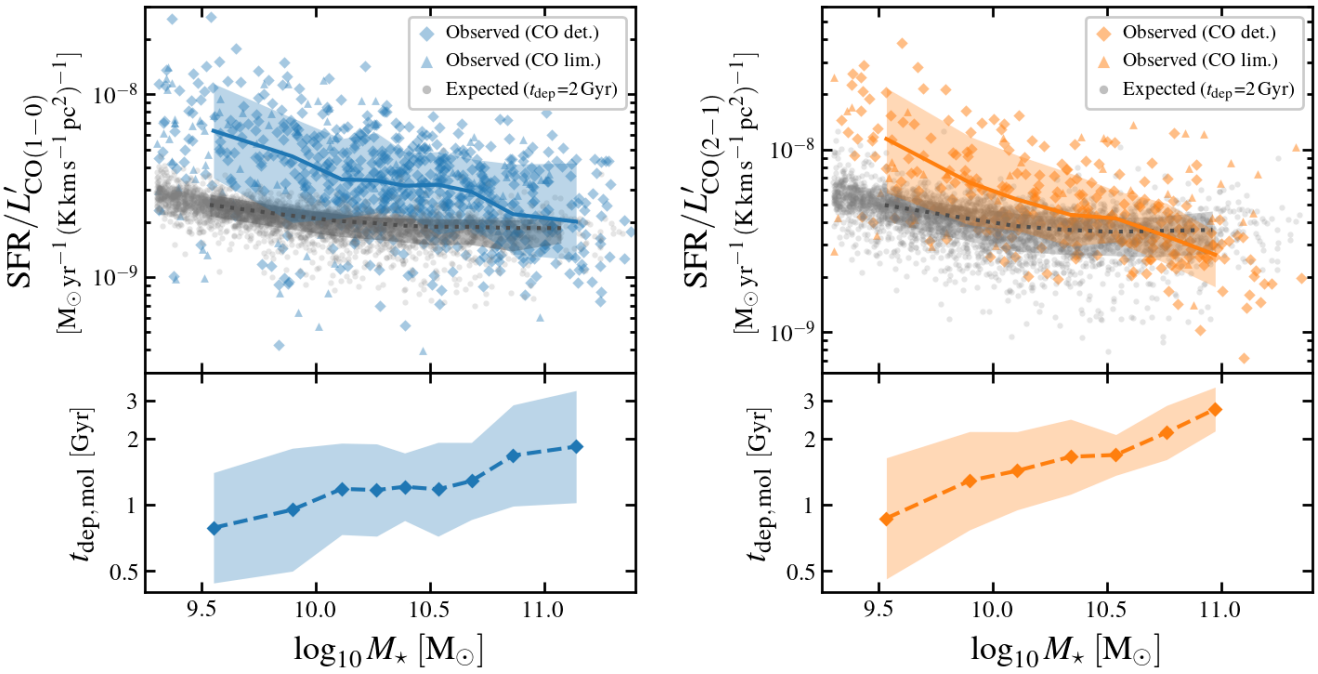


**Figure 7.** Galaxy-integrated SFR to CO luminosity ratios as a function of stellar mass (*top*) and the implied molecular gas depletion time trends (*bottom*). Results based on CO (1–0) data are shown on the left, whereas those based on CO (2–1) are on the right. In the top panels, blue/orange symbols show a large set of observational measurements (diamonds) and CO upper limits (upward triangles, corresponding to $\mathrm{SFR}/L'_{\mathrm{CO}}$ lower limits) from the literature compiled by Leroy et al. (2022, 2023). The blue/orange solid lines show the running median for these observations, and shaded regions showing the $1\sigma$ (16–84th percentile) range. Gray symbols and dotted lines instead show the *expected* relationship across our sample from our predicted global $\alpha_{\mathrm{CO}}$ values assuming a fixed molecular gas depletion time $t_{\mathrm{dep,\,fid}} = 2$ Gyr. The discrepancies between the observations (blue/orange) and the expectations (gray) can be explained if $t_{\mathrm{dep}}$ varies systematically as a function of $M_\star$. We show these implied variations in the bottom panels. The implied $t_{\mathrm{dep}}$ variations are ∼0.5 dex across the probed $M_\star$ range and 0.1–0.3 dex at a given $M_\star$.

This translates to a ∼0.3 dex difference from value at the high-mass end, which is only half of the observed range in $\mathrm{SFR}/L'_{\mathrm{CO}}$.

Alternatively, $t_{\mathrm{dep}}$ may vary as a function of $M_\star$, with lower values in low $M_\star$ systems. This appears to be the most likely explanation for our results. By contrasting the observed trends with the predicted ones, we can derive the implied variations in $t_{\mathrm{dep}}$ if our $\alpha_{\mathrm{CO}}$ predictions are accurate. These implied $t_{\mathrm{dep}}$ trends are shown in the bottom panels of Figure 7.

In detail, the overall slope discrepancies suggest that $t_{\mathrm{dep}}$ increases by ∼0.5 dex over $M_\star = 10^{9.5-11}\,\mathrm{M_\odot}$, only reaching the fiducial 2 Gyr value near the high $M_\star$ end. The best-fit power-law relations are:

$$t_{\mathrm{dep}}^{\mathrm{CO}(1-0)} = 1.2\,\mathrm{Gyr}\,(M_\star/10^{10}\,\mathrm{M_\odot})^{0.19}\,, \quad (12)$$

$$t_{\mathrm{dep}}^{\mathrm{CO}(2-1)} = 1.6\,\mathrm{Gyr}\,(M_\star/10^{10}\,\mathrm{M_\odot})^{0.29}\,. \quad (13)$$

The mild discrepancy between these trends inferred from CO (1–0) and CO (2–1) seems to suggest that our $R_{21}$ predictions may not fully account for its trends with $M_\star$ in reality, or the CO (1–0) and CO (2–1) datasets in the literature may be influenced by different systematic effects, or both.

Another way to phrase our quantitative results is that roughly 1/3 of the observed trend in $\mathrm{SFR}/L'_{\mathrm{CO}}$ with $M_\star$ are due to the predicted $\alpha_{\mathrm{CO}}$ variations, and the remaining 2/3 are due to $t_{\mathrm{dep}}$ variations. This is in reasonable agreement with results in the literature. For example, Saintonge et al. (2017) reports an anti-correlation between $t_{\mathrm{dep}}$ and $M_\star$ based on the $\alpha_{\mathrm{CO}}$ prescription of Accurso et al. (2017), and Hunt et al. (2020) find similar results based on their $\alpha_{\mathrm{CO}}$ estimates.

Exploring the reason for the shorter $t_{\mathrm{dep}}$ in low-mass galaxies is beyond the scope of this paper. However, we note that the ISM in these galaxies tends to be more dominated by H I compared to $H_2$ (e.g., Saintonge & Catinella 2022), they tend to host fewer molecular clouds with lower surface densities (e.g., Sun et al. 2022). The shorter $t_{\mathrm{dep}}$ in low-$M_\star$ galaxies may reflect that these galaxies lack diffuse or inert molecular gas, that atomic gas makes up more of the material in star-forming complexes, and/or that feedback more readily disperses molecular clouds.

## 6. SUMMARY

We analyze GALEX UV and WISE IR images for 10,657 local galaxies to measure the UV-to-IR surface brightness radial profiles, half-light radii, stellar mass surface density ($\Sigma_\star$) profiles, and SFR surface density ($\Sigma_{\rm SFR}$) profiles for those detected in the relevant bands. This represents a major effort to systematically characterize the radial structure of massive galaxies ($M_\star > 10^{9.3}\,{\rm M}_\odot$) throughout the local volume ($d \lesssim 50$ Mpc), as part of the $z$=0 Multiwavelength Galaxy Synthesis project (Leroy et al. 2019).

While these measurements have broad relevance and many potential applications, in this work we primarily use them to obtain CO-to-$H_2$ conversion factor ($\alpha_{\rm CO}$) predictions based on state-of-the-art empirical prescriptions (e.g., Bolatto et al. 2013; Gong et al. 2020; Schinnerer & Leroy 2024). These spatially resolved $\alpha_{\rm CO}$ predictions cover 5,244 galaxies, many of which have been (or will likely be) targeted in large CO mapping campaigns. Our $\alpha_{\rm CO}$ predictions address the urgent need for modern CO studies to account for substantial $\alpha_{\rm CO}$ variations both within a galaxy and among galaxies.

To validate our $\alpha_{\rm CO}$ predictions, we compile existing observational $\alpha_{\rm CO}$ measurements in the literature (including dust-based, CO multi-line modeling, and carbon budget accounting results; Sandstrom et al. 2013; Israel 2020; den Brok et al. 2023a; Teng et al. 2023; Yasuda et al. 2023; Chiang et al. 2024), and check our predictions against these measurements for a small overlapping subsample of galaxies (Figure 3 and Figure 4). The best agreements are achieved when the predictions account for not only CO-dark gas (as a function of metallicity), but also CO emissivity (as a function of $\Sigma_\star$) and excitation effects (as a function of $\Sigma_{\rm SFR}$). The emissivity effects are crucial for properly reproducing the observed low $\alpha_{\rm CO}$ values in the inner regions of massive galaxies, although there remains some tension between different observational measurements in this regime. The excitation effects play a central role in translating between CO transitions and should be considered when using CO (2–1) or higher-$J$ lines to trace molecular gas.

Across our entire sample, the $\alpha_{\rm CO}$ predictions exhibit several salient trends as functions of galaxy global stellar mass ($M_\star$) and SFR (Figure 5 and Figure 6). For low-$M_\star$ galaxies, the metallicity-dependent CO-dark term dominates the hybrid Schinnerer & Leroy (2024) prescription, predicting high values of $\alpha_{\rm CO(1-0)} \gtrsim 5$ and $\alpha_{\rm CO(2-1)} \gtrsim 10$ (in units of ${\rm M}_\odot\ {\rm pc}^{-2}\ ({\rm K\ km\ s}^{-1})^{-1}$). For high-$M_\star$ but low-SFR galaxies, the $\Sigma_\star$-dependent emissivity term becomes prominent and predicts low values of $\alpha_{\rm CO(1-0)} \lesssim 2.5$ and $\alpha_{\rm CO(2-1)} \lesssim 5$. For high-SFR galaxies, the $\Sigma_{\rm SFR}$-dependent excitation term predicts high CO (2–1)-to-(1–0) ratios of $R_{21} \gtrsim 0.8$, which suggests lower $\alpha_{\rm CO(2-1)}$ values even though $\alpha_{\rm CO(1-0)}$ may be moderate.

We explore the implications of our prediction for the molecular gas depletion time, $t_{\rm dep}$ (Figure 7). Leveraging an extensive compilation of galaxy global SFR and CO luminosity measurements, we measure the dependence of ${\rm SFR}/L'_{\rm CO}$ on $M_\star$ for main sequence galaxies to be ${\rm SFR}/L'_{\rm CO(1-0)} \propto M_\star^{-0.29}$ and ${\rm SFR}/L'_{\rm CO(2-1)} \propto M_\star^{-0.40}$. We contrast these measurements with expectations from our $\alpha_{\rm CO}$ predictions and a fixed $t_{\rm dep}$, finding that the observed trends are much stronger than the expected trends and exhibit $\sim$3 times wider range of ${\rm SFR}/L'_{\rm CO}$ values over the same $M_\star$ range. The most likely explanation is that the molecular gas depletion time increases systematically with $M_\star$, from $\lesssim$1 Gyr at $M_\star = 10^{9.5}\,{\rm M}_\odot$ to 2–3 Gyr at $10^{11}\,{\rm M}_\odot$.

We believe this work offers the best attempt to date in quantifying the radial structures of and $\alpha_{\rm CO}$ variations in galaxies throughout the local universe. To facilitate many potential applications of our results, we publish all measurements from this work in the form of machine-readable tables (including resolved radial profiles as well as global values, see subsection 4.2) and FITS images ($\alpha_{\rm CO}$ predictions for galaxies in several CO surveys, see Appendix C). We also publish a `Python` package that compiles and implements many empirical $\alpha_{\rm CO}$ prescriptions in the literature (Appendix D). We hope that these efforts will motivate the community to adopt current best practices for handling $\alpha_{\rm CO}$ (especially in the context of large CO surveys, e.g., EDGE-CALIFA, PHANGS, MAUVE, and KILOGAS; Bolatto et al. 2017; Leroy et al. 2021a, J. Sun et al., in preparation), but also to expand and improve the current set of $\alpha_{\rm CO}$ measurements from observations.

JS acknowledges support by the National Aeronautics and Space Administration (NASA) through the NASA Hubble Fellowship grant HST-HF2-51544 awarded by the Space Telescope Science Institute (STScI), which is operated by the Association of Universities for Research in Astronomy, Inc., under contract NAS 5-26555. YHT and ADB acknowledge support from grant NSF-AST 2307441. AKL and RC gratefully acknowledge support from NSF AST AWD 2205628, JWST-GO-02107.009-A, and JWST-GO-03707.001-A. AKL also gratefully acknowledges support by a Humboldt Research Award. AH acknowledges support by the Programme National Cosmology et Galaxies (PNCG) of CNRS/INSU with INP and IN2P3, co-funded by CEA and CNES, and by the Programme National Physique et Chimie du Milieu Interstellaire (PCMI) of CNRS/INSU with INC/INP co-funded by CEA and CNES.

The z0MGS project and the creation of the GALEX and WISE atlas was supported by NASA ADAP grants NNX16AF48G and NNX17AF39G and National Science Foundation grant No. 1615728. The *GALEX* and *WISE* data used in this paper can be found in the NASA/IPAC Infrared Science Archive: 10.26131/IRSA6.

This work is based in part on observations made with the *Galaxy Evolution Explorer (GALEX)*. *GALEX* is a NASA Small Explorer, whose mission was developed in cooperation with the Centre National d'Etudes Spatiales (CNES) of France and the Korean Ministry of Science and Technology. *GALEX* is operated for NASA by the California Institute of Technology under NASA contract NAS5-98034.

This work makes use of data products from the *Wide-field Infrared Survey Explorer (WISE)*, which is a joint project of the University of California, Los Angeles, and the Jet Propulsion Laboratory/California Institute of Technology, funded by NASA.

This paper has made use of the SAO/NASA Astrophysics Data System[14], funded by NASA under Cooperative Agreement 80NSSC21M00561. We also acknowledge the usage of the HyperLEDA database[15].

*Facilities:* GALEX, WISE, ALMA, APEX, ARO:12m, ARO:SMT, CARMA, FCRAO, IRAM:30m, No:45m

*Software:* `NumPy` (Harris et al. 2020), `SciPy` (Virtanen et al. 2020), `Matplotlib` (Hunter 2007), `Astropy` (Astropy Collaboration et al. 2013, 2018, 2022), `APLpy` (Robitaille & Bressert 2012), `CO_conversion_factor` (https://github.com/astrojysun/COConversionFactor), `adstex` (https://github.com/yymao/adstex).

# APPENDIX

## A. STRIPE INTEGRAL

We use a "stripe integral" method (Warmels 1988) to reconstruct surface brightness radial profiles for galaxies with high inclination angles (see subsection 2.2). In this appendix, we detail the concept behind this method, our implementation, and some caveats.

Figure A1 illustrates the concept with an inclined galaxy disk that is geometrically thin, axisymmetric, and has optically thin emission. This distribution, when viewed face-on, follows a surface brightness radial profile, $I(r)$. A common way to derive $I(r)$ for moderately inclined galaxies is to calculate the average observed surface brightness in a series of radial bins and multiply them by $\cos i$ to account for the inclination. This is the "radial binning" method, and the result would be a series of inclination-corrected surface brightnesses $(I_1, I_2, ..., I_n)$ as a discrete representation of the true surface brightness profile $I(r)$.

The radial binning method works under three conditions: (a) the inclination and position angle of the galaxy are well known, (b) the light distribution along the (projected) minor axis is well resolved in observations, and (c) the intrinsic "flatness" of the galaxy disk, defined as the disk vertical scale height to radial scale length ratio, is much smaller than $\cos i$. For high-inclination galaxies that do not fulfill these conditions, there will be substantial "smearing" of emission along the minor axis across radial bins, such that the radial binning measurements become at least inaccurate, if not completely meaningless. In the case where the inclination is poorly constrained, the conversion to face-on surface brightness estimates will also be highly uncertain.

The stripe integral method reconstructs $I(r)$ even in cases where these conditions do not hold. Instead of radial bins, it defines a series of rectangular "integration stripes," each spanning the full width of the galaxy along its minor axis (see bottom part of Figure A1). The width of these integration stripes along the major axis matches the desired radial bin width for the output surface brightness profile, and the stripes collectively cover the entire galaxy footprint. Within each stripe, one computes the enclosed total flux density, $S = \int I d\Omega$. This sequence of integrated flux densities across all stripes $(S_1, S_2, ..., S_n)$ represents a key intermediate product.

Under the assumptions of an axisymmetric disk, optically thin emission, and no emission beyond the last

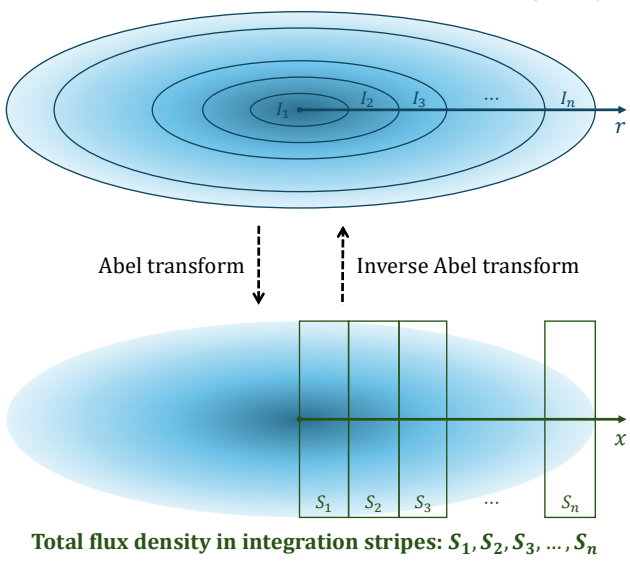


**Figure A1.** Illustration of a surface brightness profile measured from radial binning $(I_1, I_2, ..., I_n$; *top*) and a flux density sequence computed via stripe integrals $(S_1, S_2, ..., S_n$; *bottom*). For axisymmetric disks, they are related by a discrete version of the Abel transform (or its inverse).

[14] https://ui.adsabs.harvard.edu/
[15] http://atlas.obs-hp.fr/hyperleda/

radial bin, one can translate between the radial surface brightness profile $I_1, I_2, ..., I_n$ and the flux density sequence $S_1, S_2, ..., S_n$ via a discrete version of the Abel transform (or its inverse transform). For such linear transforms between $n$-dimensional vectors, one can write them in matrix form as:

$$\begin{bmatrix} S_1 \\ S_2 \\ \vdots \\ S_n \end{bmatrix} = A \begin{bmatrix} I_1 \\ I_2 \\ \vdots \\ I_n \end{bmatrix}, \quad \text{or} \quad \begin{bmatrix} I_1 \\ I_2 \\ \vdots \\ I_n \end{bmatrix} = A^{-1} \begin{bmatrix} S_1 \\ S_2 \\ \vdots \\ S_n \end{bmatrix}. \quad \text{(A1)}$$

Here, $A$ is the matrix representation of the Abel transform. Its matrix elements $A_{ij}$ can be interpreted geometrically as the (deprojected) overlapping area between the $i$th integration stripe and the $j$th radial bin. Given the number of stripes/bins and their width in angular units, one can calculate all the matrix elements according to this geometric interpretation. One can then compute the inverse of $A$ and use it to convert the flux density sequence $S_1, S_2, ..., S_n$ to the radial surface brightness profile $I_1, I_2, ..., I_n$.

We note that this matrix-based implementation differs from the iterative approach adopted by Warmels (1988). There, the radial surface brightness profile is solved iteratively using the Richardson–Lucy algorithm (Richardson 1972; Lucy 1974). While this algorithm has desirable features such as enforcing nonnegative surface brightness and remaining robust against noise, its computational cost becomes non-negligible when applied to thousands of galaxies with six-band images at different resolutions. Our matrix-based implementation is much less computation-intensive and thus more practical when dealing with a large galaxy sample, as is the case with this study.

To account for the effect of noise, we calculate the measurement errors on the stripe-integrated flux densities $S_1, S_2, ..., S_n$, propagate them to the output surface brightness profile $I_1, I_2, ..., I_n$, and truncate the profile where the S/N ratio per bin drops below 3. The effect of noise accumulates from large to small galactocentric radius in this setup. As a result, the surface brightness profile derived from stripe integral often drops below S/N = 3 at smaller radii compared to that derived from direct radial binning for low-inclination galaxies.

Another notable caveat when applying the stripe integral method to our data is the presence of pixels masked due to the presence of foreground stars or background galaxies (see subsection 2.1) and outlier pixels (e.g., unmasked stars). For masked pixels, we cannot simply assign them the mean or median of the unmasked pixels in a stripe because we do not expect those pixels to have similar surface brightnesses (this differs from the case of radial binning). For unmasked stars, the effect of these outliers can accumulate and end up affecting the output surface brightness profile across all inner radial bins.

To address these issues, we prepare the images in the following way before calculating the stripe integral: for each pixel in the image, we find its reflection about the galaxy center, major axis, and minor axis, and use the median among these four pixels (ignoring masked pixels) to replace the original pixel value. This step leverages the four-fold symmetry about the galaxy axes expected for axisymmetric galaxy disks at all inclination angles. It allows for filling in masked pixels in a reasonable way and reduces the impact of outlier pixels on the stripe integral calculation because they contribute only 1 of 4 points in the median. For moderately inclined galaxies, we generally see better agreement between the stripe integral-based results and radial binning after implementing this preparatory step, which confirms its effectiveness.

## B. RESOLUTION EFFECTS

One of the key intermediate measurements in this work is the galaxy half-light radius, $r_{50}$, which we derive from the radial surface brightness profile for each band (see subsubsection 2.2.1). This measurement can be affected by the finite resolution of the images, especially when the target galaxy is small and its radial profile is not fully resolved. In this appendix, we assess this effect by analyzing images of mock galaxies with varying sizes and inclination angles and quantifying the systematic biases due to resolution limit.

We create a set of mock images of galaxies. Each model is an axisymmetric disk with an exponential surface brightness profile, but with varying galaxy sizes and inclination angles. The ratio of the galaxy size, determined by the exponential scale length ($r_{\rm scale,\,true}$), to the PSF size ($\theta_{\rm PSF}$), determines how well the galaxy is resolved. We define a grid that spans $r_{\rm scale,\,true}/\theta_{\rm PSF} = 0.1-5.0$, from unresolved to well resolved. Our grid of inclinations spans $i = 0°-85°$, i.e., from face-on to almost edge-on.

For each combination of $r_{\rm scale,\,true}/\theta_{\rm PSF}$ and $i$, we project a disk with an exponential surface brightness profile onto the sky plane and convolve it with the appropriate Gaussian PSF to create a mock image. We then measure its surface brightness profile via both the radial binning and stripe integral approaches, and so derive the half-light radius ($r_{50,\,\rm obs}$) in the same way as we would for a real galaxy (see subsection 2.2). By comparing the observed $r_{50,\,\rm obs}$ and true value $r_{50,\,\rm true} \approx 1.68\, r_{\rm scale,\,true}$ for each mock galaxy, we measure the systematic bias imposed by finite resolution.

The left panel in Figure B2 shows the results of these experiments. As expected, the ratio of observed to true galaxy size ($r_{50,\,\rm obs}/r_{50,\,\rm true}$) is close to unity in the well-resolved regime, i.e., $r_{\rm scale,\,true}/\theta_{\rm PSF} > 2$. The galaxy size becomes increasingly overestimated at smaller $r_{50,\,\rm true}/\theta_{\rm PSF}$, reaching a factor of 2 at $r_{\rm scale,\,true}/\theta_{\rm PSF} \approx 0.2-0.4$. The colored lines show a secondary dependence on the inclination angle when

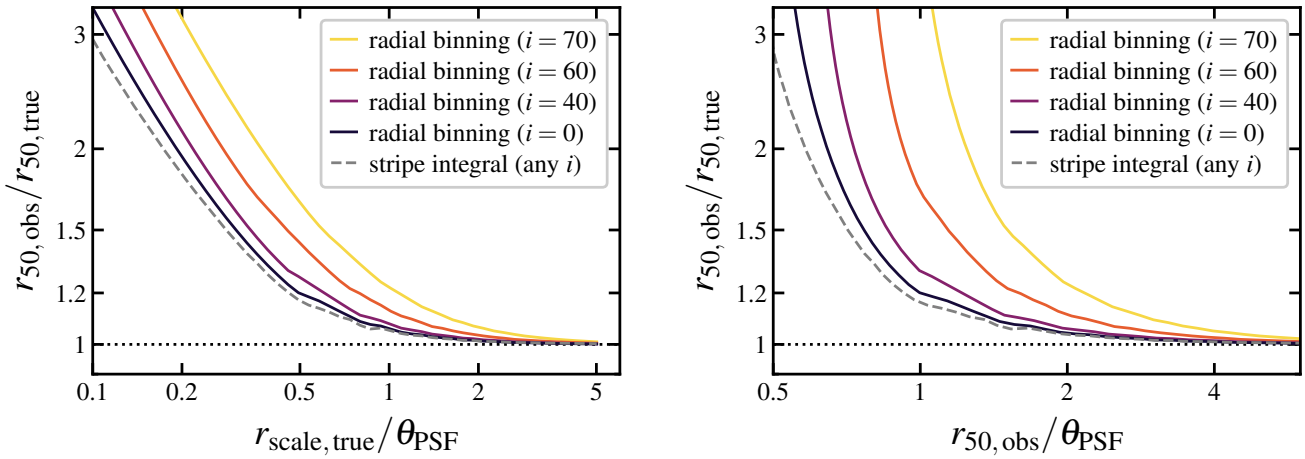


**Figure B2.** Effects of finite data resolution on galaxy half-light radius ($r_{50}$) measurements. The $y$-axes show the discrepancy between the observed half-light radius ($r_{50,\mathrm{obs}}$) and the true value ($r_{50,\mathrm{true}}$), which diminishes as the galaxy becomes better resolved (towards larger $x$ values). The $x$-axis represents the ratio of galaxy exponential scale radius ($r_{\mathrm{scale,true}}$) over PSF size ($\theta_{\mathrm{PSF}}$) in the left panel, or the ratio of the observed effective radius ($r_{50,\mathrm{obs}}$) over PSF size in the right panel. When measuring $r_{50}$ with the direct radial binning method (see subsection 2.2), resolution-induced discrepancies are more substantial for more inclined galaxies (brighter colored lines); in contrast, $r_{50}$ measured via the stripe integral method (see subsection 2.2 and Appendix A) is insensitive to galaxy inclination. Results shown by the right panel can be used to correct for resolution-induced biases in $r_{50}$, as both $r_{50,\mathrm{obs}}/\theta_{\mathrm{PSF}}$ ($x$-axis) and $i$ (color-code) are directly measurable from observations.

measuring the surface brightness profile via radial binning. As expected, we observe no dependence of $r_{50,\mathrm{obs}}/r_{50,\mathrm{true}}$ on the inclination when inferring $r_{50,\mathrm{obs}}$ using the stripe integral technique.

Based on these results, we correct our galaxy size measurements for resolution-induced bias. To do this, we first recast our model ($r_{\mathrm{scale,true}}/\theta_{\mathrm{PSF}}$, $i$) grid into a ($r_{50,\mathrm{obs}}/\theta_{\mathrm{PSF}}$, $i$) grid, in which both parameters can be measured from observations. This is done by calculating $r_{50,\mathrm{obs}}/\theta_{\mathrm{PSF}} = (r_{50,\mathrm{obs}}/r_{50,\mathrm{true}}) \times (1.68\, r_{\mathrm{scale,true}}/\theta_{\mathrm{PSF}})$ for each node in the model grid. Then we interpolate the $r_{50,\mathrm{obs}}/r_{50,\mathrm{true}}$ values from the model grid nodes (see Figure B2 right panel) to cover the corresponding ($r_{50,\mathrm{obs}}/\theta_{\mathrm{PSF}}$, $i$) space spanned by our grid. At high $r_{50,\mathrm{obs}}/\theta_{\mathrm{PSF}} > 5$ i.e., outside our measured grid, we treat $r_{50,\mathrm{obs}}$ as the true value, since virtually no correction is required. At low $r_{50,\mathrm{obs}}/\theta_{\mathrm{PSF}}$, we truncate the interpolated values at $r_{50,\mathrm{obs}}/r_{50,\mathrm{true}} = 2$, beyond which this correction factor becomes too large and too sensitive to small variations in the input parameter. In those cases, we deem it impossible to robustly recover the true galaxy size $r_{50,\mathrm{true}}$ from the observations.

## C. CONVERSION FACTOR MAPS

We provide two-dimensional predicted $\alpha_{\mathrm{CO}}$ maps for several modern CO surveys, including COMING (Sorai et al. 2019), HERACLES (Leroy et al. 2009), PHANGS–ALMA (Leroy et al. 2021a), and VERTICO (Brown et al. 2021). To maximize the utility of these maps, we refine the data processing for each sample by (1) updating key galaxy parameters (e.g., inclination and position angles) to match the adopted values in the corresponding survey papers, (2) matching the WCS grids of the $\alpha_{\mathrm{CO}}$ maps to the CO maps published by each survey, and (3) visually inspecting all products and making additional adjustments when necessary. These maps, together with other data products from this project, will be publicly available in a Canadian Astronomy Data Centre (CADC) archive.

We also considered other local galaxy CO surveys such as AlFoCS (Zabel et al. 2019), ALMaQUEST (Lin et al. 2020), CARMA–EDGE (Bolatto et al. 2017), and the Fornax ACA survey (Morokuma-Matsui et al. 2022). However, the overlaps between these samples and ours are limited due to mismatches in the sample selection criteria, i.e., the distance range (for ALMaQUEST and CARMA–EDGE) or stellar mass cutoff (for the Fornax surveys). Since the selection of $z$0MGS is driven by the resolution and sensitivity of WISE, this implies that other data sets are likely better suited to underpin conversion factor estimates for those surveys. Therefore, we consider that creating conversion factor maps for these samples is beyond the scope of this work and more suitable for dedicated follow-up efforts.

## D. PYTHON IMPLEMENTATION OF CONVERSION FACTOR PRESCRIPTIONS

We provide `CO_conversion_factor`, a `Python` package that is `pip`-installable[16] and compiles many existing CO-to-$H_2$ conversion factor prescriptions in the literature. In addition to the prescriptions used in this

[16] https://pypi.org/project/CO-conversion-factor/

work (Bolatto et al. 2013; Gong et al. 2020; Schinnerer & Leroy 2024), the compilation also includes Narayanan et al. (2012), Amorín et al. (2016), Accurso et al. (2017), Sun et al. (2020), and Teng et al. (2024). Each prescription (or family of prescriptions) is implemented as a stand-alone `Python` function that takes a set of input parameters relevant to the prescription (such as metallicity or gas mass surface density) and returns its conversion factor prediction. Note that these prescriptions are often calibrated within a finite range of input parameters. Their applications should therefore be limited to within the same range of parameter space.

Since metallicity is the most common input parameter for these prescriptions, but the covering fraction of high-quality metallicity measurements remains low among nearby galaxies, the package also includes the scaling relation-based metallicity prescriptions used in this work (subsection 2.3). These prescriptions leverage galaxy mass-metallicity relations and metallicity radial gradients measured in large surveys like CALIFA or SAMI (Sánchez et al. 2014, 2017, 2019). We recommend using these prescriptions only when direct observational measurements are not available.

## REFERENCES


Accurso, G., Saintonge, A., Catinella, B., et al. 2017, MNRAS, 470, 4750

Amorín, R., Muñoz-Tuñón, C., Aguerri, J. A. L., & Planesas, P. 2016, A&A, 588, A23

Asplund, M., Grevesse, N., Sauval, A. J., & Scott, P. 2009, ARA&A, 47, 481

Astropy Collaboration, Robitaille, T. P., Tollerud, E. J., et al. 2013, A&A, 558, A33

Astropy Collaboration, Price-Whelan, A. M., Sipőcz, B. M., et al. 2018, AJ, 156, 123

Astropy Collaboration, Price-Whelan, A. M., Lim, P. L., et al. 2022, ApJ, 935, 167

Barrera-Ballesteros, J. K., Utomo, D., Bolatto, A. D., et al. 2020, MNRAS, 492, 2651

Bolatto, A. D., Wolfire, M., & Leroy, A. K. 2013, ARA&A, 51, 207

Bolatto, A. D., Wong, T., Utomo, D., et al. 2017, ApJ, 846, 159

Bothwell, M. S., Wagg, J., Cicone, C., et al. 2014, MNRAS, 445, 2599

Brown, T., Wilson, C. D., Zabel, N., et al. 2021, ApJS, 257, 21

Catinella, B., Cortese, L., Sun, J., et al. 2025, The Messenger, submitted

Chiang, I.-D., Sandstrom, K. M., Chastenet, J., et al. 2024, ApJ, 964, 18

Chown, R., Li, C., Parker, L., et al. 2021, MNRAS, 500, 1261

Cicone, C., Bothwell, M., Wagg, J., et al. 2017, A&A, 604, A53

Colombo, D., Sanchez, S. F., Bolatto, A. D., et al. 2020, A&A, 644, A97

Colombo, D., Kalinova, V., Bazzi, Z., et al. 2025, arXiv e-prints, arXiv:2507.06375

Davis, T. A., Greene, J. E., Ma, C.-P., et al. 2019, MNRAS, 486, 1404

den Brok, J., Oakes, E., Leroy, A., et al. 2025, ApJ submitted

den Brok, J. S., Chatzigiannakis, D., Bigiel, F., et al. 2021, MNRAS, 504, 3221

den Brok, J. S., Bigiel, F., Chastenet, J., et al. 2023a, A&A, 676, A93

den Brok, J. S., Leroy, A. K., Usero, A., et al. 2023b, MNRAS, 526, 6347

Donovan Meyer, J., Koda, J., Momose, R., et al. 2013, ApJ, 772, 107

Downes, D., & Solomon, P. M. 1998, ApJ, 507, 615

Dunne, L., Maddox, S. J., Papadopoulos, P. P., Ivison, R. J., & Gomez, H. L. 2022, MNRAS, 517, 962

Faustino Vieira, H., Duarte-Cabral, A., Davis, T. A., et al. 2024, MNRAS, 527, 3639

Forbrich, J., Lada, C. J., Viaene, S., & Petitpas, G. 2020, ApJ, 890, 42

Fukui, Y., & Kawamura, A. 2010, ARA&A, 48, 547

Gao, Y., Tan, Q.-H., Gao, Y., et al. 2022, ApJ, 940, 133

Gao, Y., Xiao, T., Li, C., et al. 2019, ApJ, 887, 172

Genzel, R., Tacconi, L. J., Combes, F., et al. 2012, ApJ, 746, 69

Glenn, J., Bradford, C., Pope, A., et al. 2023, in American Astronomical Society Meeting Abstracts, Vol. 241, American Astronomical Society Meeting Abstracts, 160.08

Glover, S. C. O., & Clark, P. C. 2012, MNRAS, 421, 116

Glover, S. C. O., & Mac Low, M. M. 2011, MNRAS, 412, 337

Gong, M., Ostriker, E. C., & Kim, C.-G. 2018, ApJ, 858, 16

Gong, M., Ostriker, E. C., Kim, C.-G., & Kim, J.-G. 2020, ApJ, 903, 142

Gratier, P., Braine, J., Schuster, K., et al. 2017, A&A, 600, A27

Harris, C. R., Millman, K. J., van der Walt, S. J., et al. 2020, Nature, 585, 357

He, H., Wilson, C. D., Sun, J., et al. 2024, arXiv e-prints, arXiv:2401.16476
Helfer, T. T., Thornley, M. D., Regan, M. W., et al. 2003, ApJS, 145, 259
Heyer, M., & Dame, T. M. 2015, ARA&A, 53, 583
Holland, W. S., Bintley, D., Chapin, E. L., et al. 2013, MNRAS, 430, 2513
Hu, C.-Y., Schruba, A., Sternberg, A., & van Dishoeck, E. F. 2022, ApJ, 931, 28
Hunt, L. K., Tortora, C., Ginolfi, M., & Schneider, R. 2020, A&A, 643, A180
Hunter, J. D. 2007, Computing in Science and Engineering, 9, 90
Israel, F. P. 2020, A&A, 635, A131
Jameson, K. E., Bolatto, A. D., Leroy, A. K., et al. 2016, ApJ, 825, 12
Jiang, X.-J., Wang, Z., Gu, Q., Wang, J., & Zhang, Z.-Y. 2015, ApJ, 799, 92
Keenan, R. P., Marrone, D. P., & Keating, G. K. 2024a, arXiv e-prints, arXiv:2409.03963
—. 2025, arXiv e-prints, arXiv:2507.18823
Keenan, R. P., Marrone, D. P., Keating, G. K., et al. 2024b, ApJ, 975, 150
Komugi, S., Sawada, T., Koda, J., et al. 2025, ApJ, 980, 126
Kreckel, K., Groves, B., Schinnerer, E., et al. 2013, ApJ, 771, 62
Kreckel, K., Ho, I. T., Blanc, G. A., et al. 2019, ApJ, 887, 80
Kuno, N., Sato, N., Nakanishi, H., et al. 2007, PASJ, 59, 117
Lee, A. M., Koda, J., Egusa, F., et al. 2025, arXiv e-prints, arXiv:2507.13498
Leroy, A. K., Walter, F., Brinks, E., et al. 2008, AJ, 136, 2782
Leroy, A. K., Walter, F., Bigiel, F., et al. 2009, AJ, 137, 4670
Leroy, A. K., Bolatto, A., Gordon, K., et al. 2011, ApJ, 737, 12
Leroy, A. K., Walter, F., Sandstrom, K., et al. 2013, AJ, 146, 19
Leroy, A. K., Sandstrom, K. M., Lang, D., et al. 2019, ApJS, 244, 24
Leroy, A. K., Schinnerer, E., Hughes, A., et al. 2021a, ApJS, 257, 43
Leroy, A. K., Hughes, A., Liu, D., et al. 2021b, ApJS, 255, 19
Leroy, A. K., Rosolowsky, E., Usero, A., et al. 2022, ApJ, 927, 149
Leroy, A. K., Bolatto, A. D., Sandstrom, K., et al. 2023, ApJL, 944, L10
Leroy, A. K., Sun, J., Meidt, S., et al. 2025, arXiv e-prints, arXiv:2502.04481
Lin, L., Ellison, S. L., Pan, H.-A., et al. 2020, ApJ, 903, 145
Lisenfeld, U., Espada, D., Verdes-Montenegro, L., et al. 2011, A&A, 534, A102
Lucy, L. B. 1974, AJ, 79, 745
Makarov, D., Prugniel, P., Terekhova, N., Courtois, H., & Vauglin, I. 2014, A&A, 570, A13
Martin, D. C., Fanson, J., Schiminovich, D., et al. 2005, ApJL, 619, L1
Morokuma-Matsui, K., Bekki, K., Wang, J., et al. 2022, ApJS, 263, 40
Narayanan, D., Krumholz, M. R., Ostriker, E. C., & Hernquist, L. 2012, MNRAS, 421, 3127
Pettini, M., & Pagel, B. E. J. 2004, MNRAS, 348, L59
Richardson, W. H. 1972, Journal of the Optical Society of America (1917-1983), 62, 55
Robitaille, T., & Bressert, E. 2012, APLpy: Astronomical Plotting Library in Python, Astrophysics Source Code Library, record ascl:1208.017
Saintonge, A., & Catinella, B. 2022, ARA&A, 60, 319
Saintonge, A., Kauffmann, G., Kramer, C., et al. 2011, MNRAS, 415, 32
Saintonge, A., Catinella, B., Tacconi, L. J., et al. 2017, ApJS, 233, 22
Salim, S., Boquien, M., & Lee, J. C. 2018, ApJ, 859, 11
Salim, S., Lee, J. C., Janowiecki, S., et al. 2016, ApJS, 227, 2
Sánchez, S. F. 2020, ARA&A, 58, 99
Sánchez, S. F., Rosales-Ortega, F. F., Jungwiert, B., et al. 2013, A&A, 554, A58
Sánchez, S. F., Rosales-Ortega, F. F., Iglesias-Páramo, J., et al. 2014, A&A, 563, A49
Sánchez, S. F., Barrera-Ballesteros, J. K., Sánchez-Menguiano, L., et al. 2017, MNRAS, 469, 2121
Sánchez, S. F., Barrera-Ballesteros, J. K., López-Cobá, C., et al. 2019, MNRAS, 484, 3042
Sandstrom, K. M., Leroy, A. K., Walter, F., et al. 2013, ApJ, 777, 5
Schinnerer, E., & Leroy, A. K. 2024, ARA&A, 62, 369
Schruba, A., Leroy, A. K., Walter, F., et al. 2012, AJ, 143, 138
Smith, M. W. L., Eales, S. A., Gomez, H. L., et al. 2012, ApJ, 756, 40
Sorai, K., Kuno, N., Muraoka, K., et al. 2019, PASJ, 71, S14
Sun, J., Leroy, A. K., Ostriker, E. C., et al. 2020, ApJ, 892, 148
Sun, J., Leroy, A. K., Rosolowsky, E., et al. 2022, AJ, 164, 43

Sun, J., Leroy, A. K., Ostriker, E. C., et al. 2023, ApJL, 945, L19
Tacconi, L. J., Genzel, R., & Sternberg, A. 2020, ARA&A, 58, 157
Tacconi, L. J., Neri, R., Genzel, R., et al. 2013, ApJ, 768, 74
Teng, Y.-H., Sandstrom, K. M., Sun, J., et al. 2022, ApJ, 925, 72
—. 2023, ApJ, 950, 119
Teng, Y.-H., Chiang, I.-D., Sandstrom, K. M., et al. 2024, ApJ, 961, 42
Viaene, S., Forbrich, J., Lada, C. J., Petitpas, G., & Faesi, C. 2021, ApJ, 912, 68
Virtanen, P., Gommers, R., Oliphant, T. E., et al. 2020, Nature Methods, 17, 261
Warmels, R. H. 1988, A&AS, 72, 427
Williams, T. G., Gear, W. K., & Smith, M. W. L. 2019, MNRAS, 483, 5135
Williams, T. G., Bureau, M., Davis, T. A., et al. 2023, MNRAS, 525, 4270
Wright, E. L., Eisenhardt, P. R. M., Mainzer, A. K., et al. 2010, AJ, 140, 1868
Wylezalek, D., Cicone, C., Belfiore, F., et al. 2022, MNRAS, 510, 3119
Yajima, Y., Sorai, K., Miyamoto, Y., et al. 2021, PASJ, 73, 257
Yasuda, A., Kuno, N., Sorai, K., et al. 2023, PASJ, 75, 743
Young, J. S., & Scoville, N. Z. 1991, ARA&A, 29, 581
Young, J. S., Xie, S., Tacconi, L., et al. 1995, ApJS, 98, 219
Young, L. M., Bureau, M., Davis, T. A., et al. 2011, MNRAS, 414, 940
Zabel, N., Davis, T. A., Smith, M. W. L., et al. 2019, MNRAS, 483, 2251